A Semi-Analytical Line Transfer (SALT) Model For Bi-conical Galactic Outflows

A THESIS
SUBMITTED TO THE FACULTY OF THE
UNIVERSITY OF MINNESOTA
BY

Cody CARR

IN PARTIAL FULLFILLMENT OF THE REQUIREMENTS
FOR THE DEGREE OF
MASTER OF SCIENCE

Dr. Claudia SCARLATA

AUGUST 2017

"Although to penetrate into the intimate mysteries of nature and thence to learn the true causes of phenomena is not allowed to us, nevertheless it can happen that a certain fictive hypothesis may suffice for explaining many phenomena."

Leonard Euler

University of Minnesota

Abstract

Claudia Scarlata
Minnesota Institute for Astrophysics

Master of Science in Astrophysics

A Semi-Analytical Line Transfer (SALT) Model For Bi-conical Galactic Outflows

by Cody CARR

We generalize the semi-analytical line transfer (SALT) model recently introduced by Scarlata and Panagia (2015) for modeling galactic outflows, to account for bi-conical geometries of various opening angles and orientations with respect to the line-of-sight to the observer, as well as generalized velocity fields. We model the absorption and emission component of the line profile resulting from resonant absorption in the bi-conical outflow. We show how the outflow geometry impacts the resulting line profile. We use simulated spectra with different geometries and velocity fields to study how well the outflow parameters can be recovered. We find that geometrical parameters (including the opening angle and the orientation) are always well recovered. The density and velocity field parameters are reliably recovered when both an absorption and an emission component are visible in the spectra. This condition implies that the velocity and density fields for narrow cones oriented perpendicular to the line of sight will remain unconstrained. To conclude, we fit the model to 10 highly compact galaxies (commonly referred to as Green Peas). We observe strong evidence for bi-conical geometries.

Acknowledgements

I would like to thank my family for their unconditional support throughout the duration of this thesis. I would like to thank the faculty at the University of Minnesota for bestowing knowledge upon me, and for providing me with the ample opportunity to do research. Last, but not least, I would like to thank my advisor, Claudia Scarlata, who initiated this project and without whose support this project would not be near as complete or comprehensive.

For my family.

Contents

List of Tables

List of Figures

Chapter 1

P Cygni Profiles and Line Driven Winds

1.1 Introduction

In this thesis, we will present a semi-analytical model capable of predicting the absorption and emission features observed in atomic spectra in the context of galactic winds. By wind we are referring to the outflow of continuously ejected material from a galaxy (Beals, 1929; Parker, 1958; Veilleux, Cecil, and Bland-Hawthorn, 2005). Although we are not the first to introduce the model, our main contribution is to adapt the model to account for bi-conical outflow geometries. The purpose of this chapter is to introduce the reader to background material which is either assumed or addressed at a more technical level in Chapter 2. We describe the theory of line driven winds, i.e., winds powered by the interaction of radiation with material in the outflow. This will provide as the theoretical basis for our model. In addition we discuss P Cygni profiles which refer to the broadening of emission and absorption features observed in spectral line profiles due to the presence of strong, galactic winds. P Cygni profiles will provide the empirical connection between our model and nature.

1.2 P Cygni Profiles

Historically, winds were first observed in the atomic spectra of stars. Early observations revealed the existence of transitions proportional to the transition line (i.e., $\Delta\lambda \propto \lambda\frac{v}{c}$), and hence were the result of Doppler broadening (Campbell, 1892). Eventually, photographic evidence revealed that this broadening was due to the expansion of outflowing material surrounding the star.

A schematic for an expanding, spherical outflow is shown in Figure 1.1. All material surrounding the radiation source will absorb and reemit radiation. The reemitted radiation that makes its way back to the observer will be added to the background or continuum radiation from the source. We will refer to the addition of this radiation to the continuum as the emission component of the spectrum. The emission component is typically divided into two parts: the blue and the red shifted component, which refers to the line-of-sight velocity of the reemitting material with respect to the observer. A portion of the redshifted reemissions will be blocked by the source. We say that this material has been occulted. Only material in front of the source will scatter radiation away from the line-of-sight. We refer to the absence of this radiation from the continuum as the absorption component. The combination of both the emission and the absorption components defines the P Cygni profile.

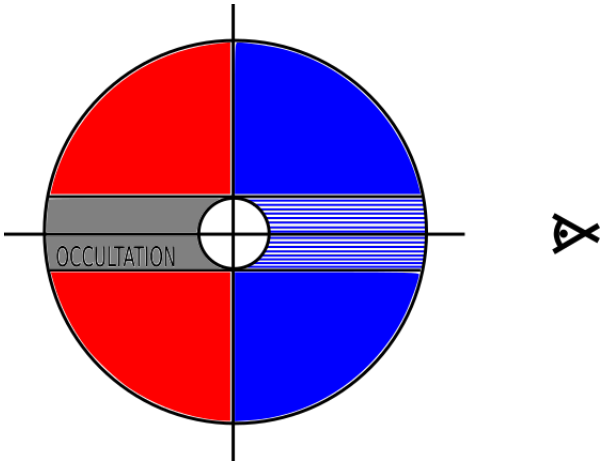

FIGURE 1.1: Cross sectional diagram of a spherical outflow as viewed from the right. Here material is outflowing radially away from an isotropically emitting source of radiation. Radiation from the source will be absorbed and reemitted by the outflow. Reemissions from behind the source (grey) will be blocked from view. Material contributing to the blue and redshifted emission components are shown by their corresponding colors. Only material between the source and the observer (lined region) will scatter photons away from the line-of-sight and contribute to the absorption component.

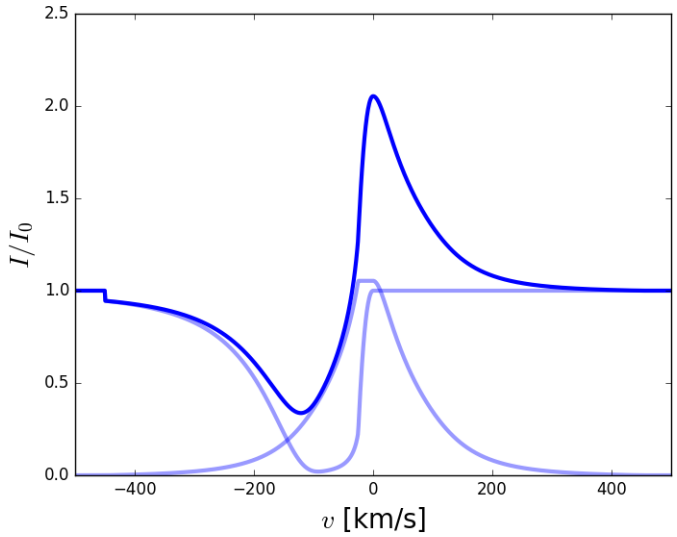

FIGURE 1.2: A normalized P Cygni profile for an atomic transition. The radiation has been normalized to the surrounding continuum. The profile is positioned in the rest frame of the transition line. The velocities represent the relative velocities of the outflow with respect to the source. Both the absorption and emission component are plotted in light blue. The emission component would naturally appear with the continuum, but the continuum has been subtracted for convenience. By definition, the redshifted emission component is associated with the positive velocity regime and the blue shifted component is with the negative velocities. Combining both the emission and absorption components produces the P Cygni profile shown in dark blue. This is what we observe and is a defining characteristic for the presence of an outflow.

A P Cygni profile along with the separate emission and absorption components is shown in Figure 1.2 for a spherical outflow. The normalized intensity of the profile is plotted with respect to the observed outflow velocity as seen by an observer in the rest frame of the transition. Note that both the absorption and emission features are broad around the center due to the Doppler shift of the outflowing material.

1.3 Line Driven Winds

In line driven winds, radiation drives outflows by transferring momentum to ions in the outflow via the absorption of photons through resonant, or ground state, electron transitions. The doppler shift is important here because it will allow radiation to continuously transfer to the outflow as material moves along a velocity gradient relative to the source of radiation. The probability of a photon scattering with ions in the outflow will depend on the optical depth of the wind, τ, or the number of mean free paths through the wind (Rybicki and Lightman, 2008). The optical depth can be written as $\tau = \int \phi k(s)\rho(s)ds$, where ρ is the density, s is distance, and k is the absorption coefficient associated with the profile function, ϕ. ϕ is defined such that $\int_0^\infty \phi(\nu)d\nu = 1$. The profile function will determine the interaction region over which a photon can be absorbed by the outflowing material. For steep velocity gradients, ϕ can be approximated as a Dirac delta function. In this case, the photon will interact, or be absorbed, only at single point in the outflow, where the relevant ion

comes exactly into resonance with the photon. This approximation is known as the Sobolev approximation (Lamers and Cassinelli, 1999) and will be used throughout the remainder of this work.

Typically, line driven winds are observed in hot, ultra luminous O and B type stars, where the bulk of the radiation is emitted in the UV and absorbed by metals in the wind (Kudritzki, 2002). Spectra of galaxies also reveal prominent P Cygni profiles in their spectra around heavy metal transition lines observed in the UV regime (Veilleux, Cecil, and Bland-Hawthorn, 2005). Under these circumstances, the stellar theory of line driven winds can be applied to galactic winds. In Chapter 2, we will use the theory of line driven winds to develop a radiation transfer model, or formerly a semi-analytical line transfer (SALT) model, to predict spectral line profiles observed in galaxies with bi-conical outflow geometries. We then fit the model to data – UV observations of highly compact (Green Pea) galaxies – in Chapter 3.

Chapter 2

Galactic SALT Model

2.1 Introduction

As a prominent source of feedback, galactic winds play a vital role in the study of galaxy evolution and the enrichment of the intergalactic medium, IGM, (Veilleux, Cecil, and Bland-Hawthorn, 2005). Observations of low-ionization and high-ionization resonant transitions in galactic winds often display P Cygni type line profiles which can reveal a wealth of information regarding the physical nature of the winds. Quantities of interest include density of the gas in the relevant ions, terminal velocity of the wind, and mass outflow rate. Galactic winds, in both the local universe (Shopbell and Bland-Hawthorn, 1998) and at higher redshift (Martin et al., 2012; Erb, 2015), appear to lack the symmetry of a full spherical outflow, and instead, are better described as having a collimated, or bi-conical geometry. The geometry of the wind can have a strong impact on the estimation of galactic properties. For example, Chisholm et al. (2016) calculated up to an order of magnitude difference in their estimate of the mass loading factor (outflow rate divided by star formation rate) in NGC 6090 when comparing a spherical to a more realistic, bi-conical model. Various groups have modeled the absorption + emission line profile resulting from the radiative transport of resonant photons in outflowing medium. Models range from simple analytic calculations (Martin et al., 2013; Scarlata and Panagia, 2015; Krumholz et al., 2017) to more advanced approaches involving Monte Carlo techniques (Prochaska, Kasen, and Rubin, 2011). In this paper, we generalize a semi-analytical line transfer (SALT) model – first introduced by Scuderi et al. (1992) in the context of stellar winds and later adapted by Scarlata and Panagia (2015) for modeling resonant lines present in galactic spectra – to account for bi-conical wind geometries and variable orientations with respect to an observer. We analyze how the geometry of the wind impacts the spectral line profile and what information can be recovered. We then test our models by fitting to P Cygni profiles generated from simulated data. We present only the theoretical description here with the intent to fit to actual galactic data in a forthcoming paper. The analytic expressions presented provide a simple way to gain physical intuition on how the wind geometry affects a line profile. This chapter is organized as follows. We begin by reviewing the SALT model, originally presented by Scarlata and Panagia (2015) for galactic outflows, in Section 2. We generalize the SALT model to bi-conical outflow geometries characterized by an opening and an orientation angle in Section 3. Our discussion follows in Section 4, where we investigate the impact of the outflow geometry on P Cygni line profiles. We test our ability to recover the wind parameters by fitting simulated data in Section 5. Finally, we present our conclusions in Section 6

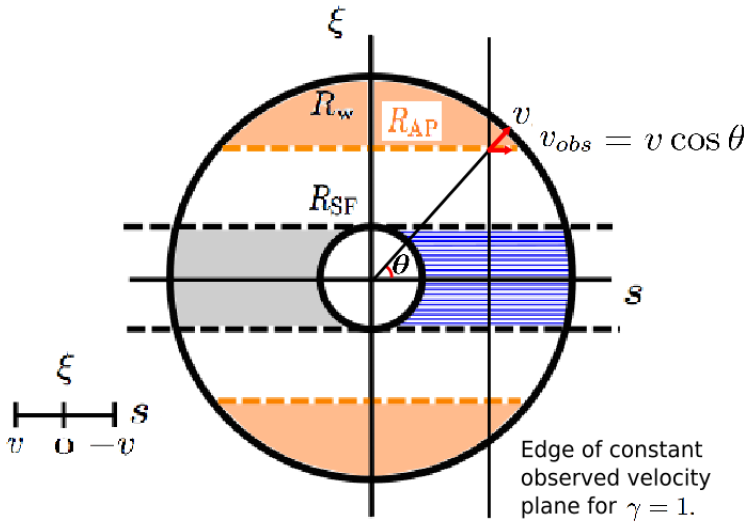

FIGURE 2.1: A cross sectional view of the spherical wind model. The line of sight is indicated by the s-axis, and the ξ-axis is in the plane of the sky. The small, central circle marks the star formation region/galaxy, with radius R_{SF}, while the outer circle indicates the extent of the wind at radius R_W. The blue shaded region indicates the absorption region – i.e., where the wind blocks the galaxy from the line of sight, whereas the white area (including the blue area) indicates the re-emission region that can be detected for a given R_{AP} (excluding the orange area). An occulted region is shaded in grey, since emission cannot be detected from behind the galaxy. In our model, the wind velocity increases monotonically with increasing radius of power law γ. A velocity vector, v, along with its observed velocity component, $v_{\rm obs}$, has been drawn in red. Velocities at and beyond R_W are equal to the terminal velocity, v_∞. The thin vertical line represents the edge of the plane of constant v_{obs} for a $\gamma = 1$ velocity field.

2.2 Spherical SALT Model

In this section, we review the SALT model introduced by Scarlata and Panagia (2015) for spherical, galactic outflows. The fiducial model consists of a spherical source (radius $R = R_{SF}$) of isotropically emitted radiation. Physically, the source embodies the star formation region/galaxy. The source is located at the center of a spherical envelope (wind) of material extending from the radius R_{SF} to the terminal radius, R_W. A schematic representation of a cross sectional cut of the envelope is presented in Figure 2.1. The ξ-axis runs perpendicular to the line of sight and is measured using normalized units, r/R_{SF}. The s-axis runs parallel with the line of sight and is measured using the same normalized units. We refer to an arbitrary radius measured in the normalized units as ρ. The wind is characterized by a velocity field, v, and a density field, n. We assume a power law for the velocity field, with:

$$\begin{aligned} v &= v_0 \left(\frac{r}{R_{\rm SF}}\right)^\gamma \quad \text{for } r < R_W \\ v &= v_\infty \qquad\qquad\quad \text{for } r \geq R_W, \end{aligned} \tag{2.1}$$

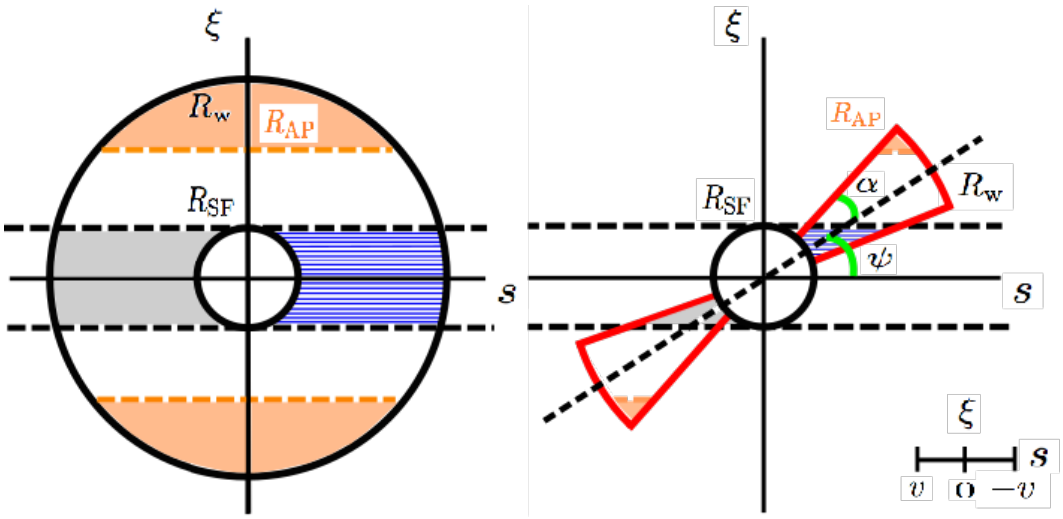

FIGURE 2.2: Cross sections for both spherical (left) and bi-conical (right) outflows. The different colored shades define the same regions as described in Figure 2.1. In both diagrams, the wind extends from the radius R_{SF} to the terminal radius R_W. The bi-conical outflow, shown in red, is defined by the orientation angle, ψ, and the opening angle, α.

where v_0 is the wind velocity at the surface of the source (i.e., at $R_{\rm SF}$), and v_∞ is the terminal velocity of the wind at R_W. Assuming a steady outflow rate, the density and velocity are related by: $n \propto (vr^2)^{-1}$. To solve the radiation transfer problem, we adopt the Sobolev's approximation (Ambartsumian, 1958; Sobolev, 1960). Provided the velocity gradient, dv/dr, is large, an atom moving with respect to the source will only absorb a photon at resonance with a transition line. Mathematically, we can approximate the profile function of the optical depth as a delta function evaluated at the Doppler shifted resonance frequency (Lamers and Cassinelli, 1999). In essence, we have reduced the radiation transfer problem to a local problem and can now decompose the outflow into thin spherical shells of a given radius, r, velocity, v, and optical depth, $\tau(r, \phi)$. Here, ϕ is the angle between the velocity and the trajectory of the photon. The optical depth is

$$\tau(r) = \frac{\pi e^2}{mc} f_{lu} \lambda_{lu} n_l(r) \left[1 - \frac{n_u g_l}{n_l g_u}\right] \frac{r/v}{1 + \sigma \cos^2 \phi}, \tag{2.2}$$

where f_{ul} and λ_{ul} are the osciallator strength and wavelength, respectively, for the ul transition, and $\sigma = \frac{{\rm d}ln(v)}{{\rm d}ln(r)} - 1$ (Castor, 1970). Assuming our density and velocity field hold, and by neglecting stimulated emission (i.e., $\left[1 - \frac{n_u g_l}{n_l g_u}\right] = 1$), we get

$$\tau(r) = \frac{\pi e^2}{mc} f_{lu} \lambda_{lu} n_0 \left(\frac{R_{\rm SF}}{r}\right)^{\gamma+2} \frac{r/v}{1 + \sigma \cos^2 \phi} \tag{2.3}$$

$$= \frac{\tau_0}{1 + (\gamma - 1) \cos^2 \phi} \left(\frac{R_{\rm SF}}{r}\right)^{2\gamma+1} \tag{2.4}$$

and

$$\tau_0 = \frac{\pi e^2}{mc} f_{lu} \lambda_{lu} n_0 \frac{R_{\rm SF}}{v_0}, \tag{2.5}$$

where $n_l(r) = n_0 \left(\frac{R_{SF}}{r}\right)^{\gamma+2}$ and n_0 is the gas density at R_{SF}. By allowing γ to vary, we will need to make a few slight modifications to several expressions presented in Scarlata and Panagia (2015), who focus on the $\gamma = 1$ scenario. For this reason, we have placed a brief review of their procedure for multiple scattering of reemitted photons in Appendix A along with our modifications. The observed spectrum needs to be computed in terms of observed velocities, $v_{\rm obs}$, which, for a given shell, is the projection of its intrinsic velocity onto the line of sight (i.e., $v_{\rm obs} = v\cos\theta$, where θ is the angle between the velocity at a given position and the line of sight). At each v_{obs}, the observed spectrum is then computed accounting for all shells that absorb and reemit at that observed velocity. For a single shell, regions of constant observed velocity form rings in the plane of the sky. Within the outflow, surfaces of constant v_{obs} can be formed by connecting all rings of the same observed velocity from neighboring shells. An infinitesimal shell will absorb a fraction $E(\tau) = 1 - e^{-\tau(v)}$ of the emitted energy. For a spherical shell, this absorbed energy will be evenly distributed in terms of the observed velocities. (We will revisit this statement later when we generalize to non-spherical outflow geometries.) • **Absorption component** To compute the absorption component of the observed spectrum, we need only concern ourselves with the portion of each shell in front of the source, as viewed on the plane of the sky (i.e., in the hatched region). A given shell can only absorb in the range of observed velocities between $[v, v_{min}]$, where $v_{\rm min}$, is the component of the velocity along the line of sight computed at $\xi = 1$. Setting $y = v/v_0$, we compute:

$$y_{\rm min} = \frac{v_{min}}{v_0} = y\cos\theta \tag{2.6}$$

$$= y^{(\gamma-1)/\gamma}(y^{2/\gamma} - 1)^{1/2}. \tag{2.7}$$

All shells with intrinsic velocity between $v_{\rm obs}$ and $v_1 = v_{\rm obs}/\cos\theta$ contribute to the absorption at v_{obs}. Setting $x = v_{\rm obs}/v_0$ and $y_1 = v_1/v_0$, one can solve the following equation to get y_1:

$$y_1^2(1 - y_1^{-2/\gamma}) = x^2. \tag{2.8}$$

Thus, the normalized absorption profile becomes

$$I(x)_{\rm abs,blue} = 1 - \int_{\rm max(x,1)}^{y_1} \frac{1 - e^{-\tau(y)}}{y - y_{\rm min}} dy, \tag{2.9}$$

where the lower bound of integration excludes the source. • **Emission component**. We have separated the emission profile into red shifted (positive velocity) and blue shifted (negative velocity) components. For both profiles, half of the remitted energy will be spread evenly from 0 to y. For a given v_{obs} in the red component, we exclude contributions from all shells where the location of v_{obs} is blocked from the observer's field of view by the source. Thus, only shells with intrinsic velocities from y_1 to $y_\infty = v_\infty/v_0$ will contribute to a given v_{obs}. The blue component will not be occulted, hence, all shells, excluding the source, will contribute. The resulting normalized profiles for the red and blue components are

$$I(x)_{\rm em,red} = \int_{y_1}^{y_\infty} \frac{1 - e^{-\tau(y)}}{2y} dy, \tag{2.10}$$

and

$$I(x)_{\rm em,blue} = \int_{\rm max(x,1)}^{y_\infty} \frac{1-e^{-\tau(y)}}{2y} dy, \tag{2.11}$$

respectively. The full P Cygni profile becomes

$$I(x) = I(x)_{\rm abs,blue} + I(x)_{\rm em,red} + I(x)_{\rm em,blue}. \tag{2.12}$$

In this formalism it is easy to account for an envelope that does not cover the full source. We define f_c as the wind covering fraction. We keep f_c constant for all shells. f_c can be thought of as clumps or small holes in the wind uniformly distributed across each shell – although the global fraction of energy absorbed by a shell is now $f_c E(\tau)$, the energy will still be evenly distributed. Lastly, we need to account for a limiting, circular observing aperture of radius, R_{AP}. Intuitively, one would expect the emission component of the spectrum to be underestimated when the aperture size is smaller than the wind. One can account for this by changing the range of integration for each profile (Scarlata and Panagia, 2015), however, the same effect can be accounted for by removing shells from the outflow using a scaling factor. We define the aperture factor

$$\Theta_{AP} \quad := \quad \Theta(y_{\rm ap} - [y^{2/\gamma} - x^2 y^{2(1-\gamma)/\gamma}]^{\gamma/2}), \tag{2.13}$$

where Θ is the Heaviside function:

$$\Theta := \begin{cases} 0 & \text{if } \ {\rm y_{ap}} < [{\rm y}^{2/\gamma} - {\rm x}^2 {\rm y}^{2(1-\gamma)/\gamma}]^{\gamma/2} \\ \\ 1 & \text{otherwise.} \end{cases} \tag{2.14}$$

$y_{ap} = v_{ap}/v_0$, where v_{ap} is the intrinsic velocity of the shell with radius R_{AP}. This scale factor will remove all shells that fall outside the aperture radius for a given, x. For an explicit derivation of Θ_{AP}, we refer the reader to Appendix B. Finally, combining the wind covering fraction, f_c, and the aperture factor, Θ_{AP}, the normalized spherical (Sp) profiles are:

$$\begin{aligned} I(x)_{\rm Sp} = \quad & 1 - \int_{\rm max(x,1)}^{y_1} \frac{\Theta_{AP} * f_c * (1-e^{-\tau(y)})}{y - y_{\rm min}} dy \\ + \quad & \int_{y_1}^{y_\infty} \frac{\Theta_{AP} * f_c * (1-e^{-\tau(y)})}{2y} dy \\ + \quad & \int_{\rm max(x,1)}^{y_\infty} \frac{\Theta_{AP} * f_c * (1-e^{-\tau(y)})}{2y} dy. \end{aligned} \tag{2.15}$$

2.3 Bi-conical SALT Model

We have constructed a bi-conical outflow with the cones' focal point positioned at the center of the source in Figure 2.2. The cones are described by two parameters: α and ψ. α is the half opening angle for each cone. We will refer to α as the opening angle. ψ is the overall angular displacement between the line of sight and the axis of the cones. We will refer to ψ as the orientation angle. A single shell of velocity v now consists of the portion of a spherical shell that lies within the bi-conical outflow.

We will refer to it as a bi-conical shell. A blue hatched section has been drawn to indicate the new absorption region. To account for a bi-conical geometry, we must consider how the energy absorbed by a given shell will be distributed in terms of the observed velocities. For a spherical shell of velocity v the energy is distributed uniformly between $\pm v$. This is demonstrated below and schematically shown in the top left panel of Figure 2.3, which shows the emission line profile for a thin spherical shell. Depending on the orientation and opening angle, a bi-conical shell with velocity v may distribute the absorbed energy over a smaller observed velocity range. In the remaining panels of Figure 2.3, we show how the line profile changes for three bi-conical shells all with the same velocity v, but different orientations and opening angles. In addition to not covering the full $\pm v$ velocity range, the energy is no longer evenly distributed. To see where the latter effect comes from, we first show why the line profile of a spherical thin shell is flat between $\pm\, v$.

Following Beals (1931), we note that the energy absorbed by a band contour, or ring of constant observed velocity (see Figure 2.4), will be proportional to the area of the band, i.e.,

$$\mathrm{d}I(v_{\mathrm{obs}})_{\mathrm{Sp}} \quad = \quad (\text{constant}) r \mathrm{d}\theta 2\pi r \sin\theta. \tag{2.16}$$

Differentiating the observed velocity, $v_{\mathrm{obs}} = -v\cos\theta$, we get

$$\mathrm{d}v_{\mathrm{obs}} \quad = \quad v \sin\theta \mathrm{d}\theta. \tag{2.17}$$

Hence,

$$\frac{\mathrm{d}I(v_{\mathrm{obs}})}{\mathrm{d}v_{\mathrm{obs}}} \quad = \quad \text{constant}, \tag{2.18}$$

and the energy is evenly distributed. In the case of a bi-conical shell the band contour will no longer be circular, i.e., at a given observed velocity, it will have an arc length, $l < 2\pi r \sin\theta$. Hence, with BC denoting the bi-conical case:

$$\mathrm{d}I(v_{\mathrm{obs}})_{\mathrm{BC}} \quad = \quad (\text{constant}) r \mathrm{d}\theta l \tag{2.19}$$

$$\implies \mathrm{d}I(v_{\mathrm{obs}})_{\mathrm{BC}} \quad = \quad \frac{l}{2\pi r \sin\theta} \mathrm{d}I(v_{\mathrm{obs}})_{\mathrm{Sp}} \tag{2.20}$$

$$\implies \frac{\mathrm{d}I(v_{\mathrm{obs}})}{\mathrm{d}v_{\mathrm{obs}}}_{\mathrm{BC}} \quad = \quad f_g \frac{\mathrm{d}I(v_{\mathrm{obs}})}{\mathrm{d}v_{\mathrm{obs}}}_{\mathrm{Sp}}, \tag{2.21}$$

where $f_g = l/2\pi r \sin\theta$. Thus, the bi-conical energy distribution can be obtained by scaling the spherical energy distribution by a scale factor, f_g. We call this scaling ratio the geometric factor. Note that the arc length, l, is a non-trivial function of the observed velocity, x, implying that the absorbed energy will no longer be evenly distributed in terms of x as in the spherical case. We have provided an explicit calculation of f_g in Appendix C.

To conclude, the normalized bi-conical profiles are:

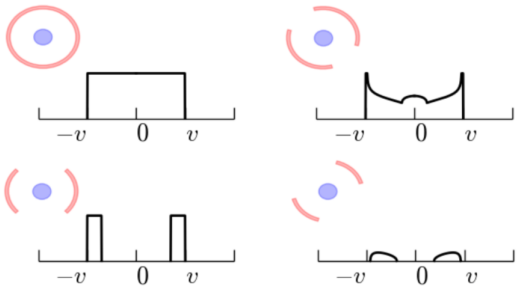

FIGURE 2.3: Single shell emission profiles for various outflow geometries, neglecting occultation from the source. Moving clockwise from the upper left, a spherical shell will absorb and reemit energy independently of v_{obs}. Thus the distribution is constant. To the right, we consider a shell with an opening angle slightly less than a sphere, oriented $45°$ away from the line of sight. At higher v_{obs}, the shell becomes indistinguishable from a full sphere. At lower v_{obs}, a bump appears in the distribution because the back end of the shell has moved between the source and the line of sight. Moving down, we consider a shell with a small opening angle, oriented $45°$ away from the line of sight. The distribution is greatly diminished, and only covers a small range in v_{obs}. Finally, at the bottom left we consider an outflow with a smaller opening angle, oriented along the line of sight. At large observed velocities, the shell cannot be distinguished from the spherical case, hence, the distribution is constant. The shell does not extend to lower v_{obs}, and there is no energy reemitted at those velocities.

$$
\begin{aligned}
I(x)_{\mathrm{BC}} = \quad & 1 - \int_{\max(x,1)}^{y_1} \frac{\Theta_{AP} * f_g * (1 - e^{-\tau(y)})}{y - y_{\min}} dy \\
& + \int_{y_1}^{y_\infty} \frac{\Theta_{AP} * f_g * (1 - e^{-\tau(y)})}{2y} dy \\
& + \int_{\max(x,1)}^{y_\infty} \frac{\Theta_{AP} * f_g * (1 - e^{-\tau(y)})}{2y} dy.
\end{aligned}
\tag{2.22}
$$

2.4 Model Discussion

We begin the discussion by investigating how the geometry of the outflow (i.e., the opening angle α and orientation angle ψ) impacts the shape of the resonant line profiles. In Figure 2.5, we vary the orientation angle while the opening angle remains fixed at $45°$. We show the absorption and emission components of the profiles separately in the left and right panels of the Figure, respectively. As ψ increases, the outflow covers a smaller fraction of the source, resulting in a smaller overall absorption. For large ψ, the absorption is limited to small observed velocities, reflecting the fact that the outermost shells (i.e., with the higher velocities) are not contributing to the absorption. For $\psi = 90°$, the outflow is oriented perpendicularly to the line of sight, and the absorption is almost negligible. At this orientation the emission component is symmetric with respect to the systemic velocity (if we ignore the

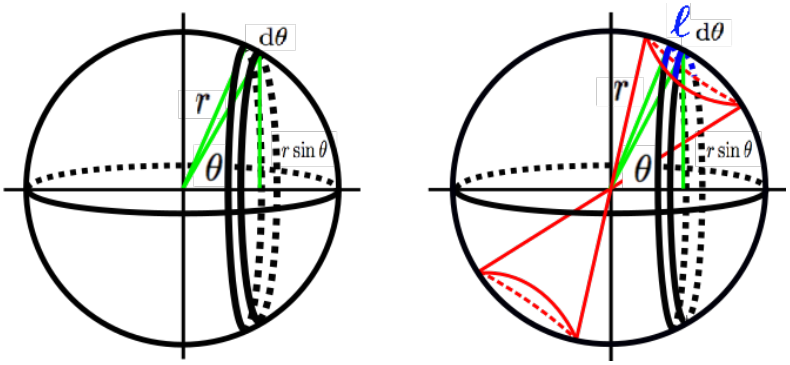

FIGURE 2.4: Band contours of constant observed velocity are shown for spherical (left) and bi-conical (right) outflows. The geometric factor, f_g, is defined as the fraction of an observed velocity contour from a spherical shell overlapping the bi-conical shell. The overlap has arc length ℓ and is shown in blue.

small occulting effect of the source). As ψ decreases and the outflow rotates towards the line of sight, gas is no longer moving perpendicularly to it. Therefore the reemission at zero velocity decreases, and a dip appears in the emission profile. The dip broadens and the emission at larger observed velocities increases as the outflow continues to move closer to the line of sight. Finally, it is important to realize that for specific inclination/opening angle combinations of the bi-conical outflow, the maximum velocity at which absorption occurs may largely underestimate the true terminal velocity of the wind. This happens when the forward facing part of the outflow is oriented in such a way that absorption no longer occurs at the terminal velocity (e.g., when $\psi > \alpha$, if $y_\infty^{1/\gamma} \sin(\psi - \alpha) > (\xi = 1)$). For these orientations, $v_{\rm max}$ only reflects the outflow geometry and orientation.

2.4.1 Line Profiles for Bi-conical Outflows

We consider the opposite scenario in Figure 2.6, where we vary the opening angle and keep the orientation angle fixed at $45°$. For $\alpha = 90°$, the geometry is spherical and the profiles are the same as presented in Scarlata and Panagia (2015). As α decreases, the outflow decreases in overall size, covering a smaller fraction of the source, leading to a smaller overall absorption component. For small α, absorption occurs only at lower velocities because the shells at larger velocity are no longer in front of the source. In the right panel, we see that for $\alpha < 90° - \psi$, material no longer moves perpendicular to the line of sight, resulting in an overall decrease in emission at zero observed velocity. The emission dip will broaden as α continues to decrease as fewer shells contribute at low velocities. Similar to Figure 2.5, the asymmetry between the blue and red emission components is due to occultation by the source. The full P Cygni profile (i.e., absorption + emission) for variable orientation angle and variable opening angle are shown in the left and right panels of Figure 2.7, respectively. These figures show that the apparent absorption component is decreased as a result of the infilling by the blue emission. However, many of the same features from the previous discussion are still visible including the emission dip. Observing such a feature would be strong evidence for a bi-conical outflow (Bae and Woo, 2016). We consider the effects of varying the velocity power law index, γ, in Figure 2.8, where we consider the spherical and bi-conical outflows in the left and right panels, respectively. In calculating the profiles we only change the

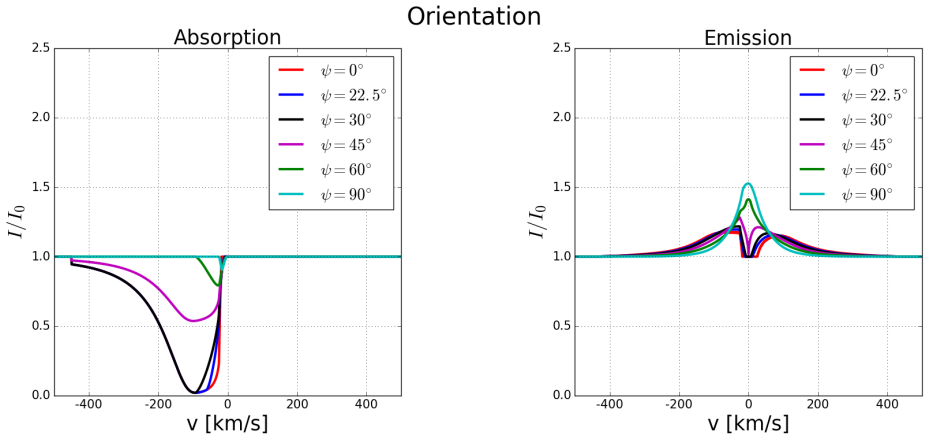

FIGURE 2.5: The opening angle, α, has been fixed at $45°$. The orientation angle, ψ, ranges from $0°$, or along the line of sight, to $90°$, or perpendicular to the line of sight. As ψ increases, the outflow is oriented away from the line of sight, resulting in fewer shells contributing to the absorption (left) and a diminished profile. As ψ decreases, more emission (right) occurs at higher velocities because the outflow is no longer perpendicular to the line of sight. For small ψ a dip will appear as no absorption occurs near zero velocity. For larger values of ψ, the outflow will be oriented perpendicular to the line of sight and a peak in emission will now occur near zero velocity. (The remaining parameters used to generate the profiles are: $\tau_0 = 330, \gamma = 1, v_0 = 25$ km/s, $\mathrm{v}_\infty = 450$ km/s.)

value of γ. In both the spherical and bi-conical cases, the strength of the absorption at high observed velocities increases with γ. This is because, as γ increases, the terminal velocity (which is constant in all models) is reached at progressively smaller distances, i.e., at progressively larger densities – resulting in stronger absorption for larger γ. Consequently, the stronger absorption is reflected in a stronger re-emission component. In the bi-conical geometry two effects are responsible for the observed line profile: 1) how quickly the density grows with respect to the velocity field, and 2) how much of the wind contributes to the emission at a given observed velocity. The first effect is controlled by γ and τ. The second effect is controlled by the geometry/orientation of the outflow and γ – which define the surfaces of constant observed velocity (see Figure B.1 in Appendix B).

2.4.2 Effects of Aperture and Covering Fraction

Spectroscopic observations are typically conducted with an aperture of finite size, which may cover only part of the scattering envelope. The shape of the resulting line profile will depend on the shape of the aperture, and on the relative sizes of the aperture and the envelope. We explore here the effects of circular apertures. We show the results for spherical and bi-conical outflows in Figure 2.9, left and right panels, respectively. The opening angle of the bi-conical outflow is fixed at $45°$ and the outflow is oriented parallel to the line of sight. As expected, for apertures smaller than the terminal radius of the wind, i.e., for $R_{AP} < R_W$, the overall emission decreases, for both the spherical and bi-conical models. The shape of the profile also changes, i.e., the decrease in emission is not a simple scaling factor. This velocity dependence is introduced by the fact that smaller apertures progressively block photons scattered by regions with different projected velocities. This effect can be clearly seen in

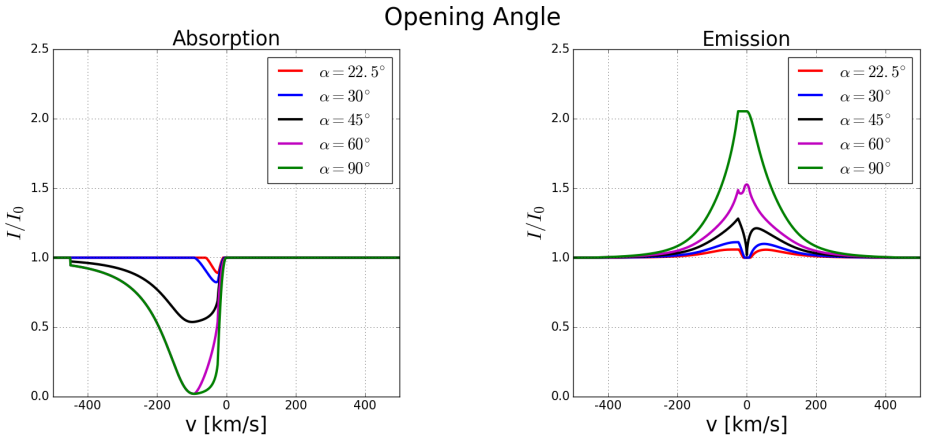

FIGURE 2.6: The orientation angle, ψ, has been fixed at $45°$. The opening angle, α, ranges from $22.5°$, or almost closed (little wind), to $90°$, which returns the spherical model. As α decreases, shells will cover a smaller fraction of the source, resulting in a diminished absorption profile (left). For small α, A dip in emission (right) occurs near zero velocity when α is small enough such that the outflow is no longer perpendicular to the line of sight. (The remaining parameters used to generate the profiles are: $\tau_0 = 330, \gamma = 1, v_0 = 25\ \mathrm{km/s}, \mathrm{v}_\infty = 450\ \mathrm{km/s}$.)

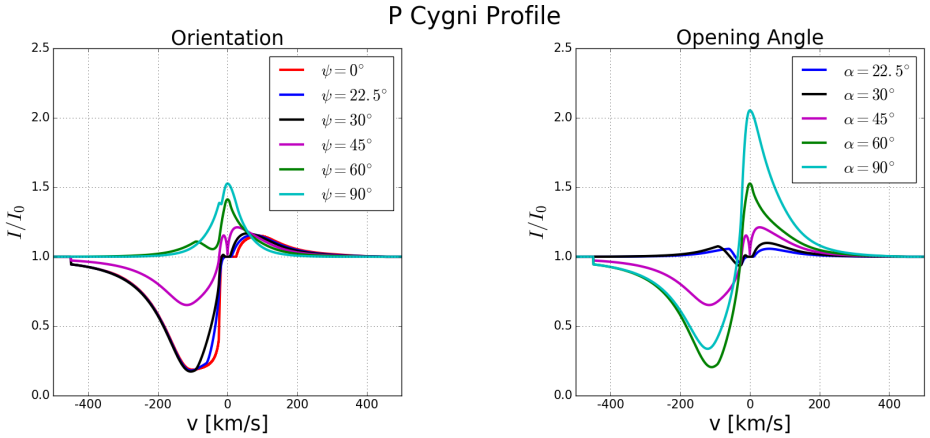

FIGURE 2.7: Resonant line transitions. In the left display, the opening angle, α, has been fixed at $45°$. The orientation angle, ψ, ranges from $0°$, or along the line of sight, to $90°$, or perpendicular to the line of sight. For smaller values of ψ, more emission occurs at higher velocities and less emission occurs near zero velocity. This is expected given the orientation of the outflow. For higher values of ψ, a peak in emission occurs near zero velocity, reflecting that the outflow is oriented perpendicularly to the line of sight. In the right display, the orientation angle, ψ, has been fixed at $45°$. The opening angle, α, ranges from $22.5°$, or almost closed (i.e., almost no wind), to $90°$, which returns the spherical model. A deficit in emission occurs near zero velocity when α is small, reflecting the fact that the outflow is no longer perpendicular to the line of sight. (The remaining parameters used to generate the profiles are: $\tau_0 = 330, \gamma = 1, v_0 = 25\ \mathrm{km/s}, \mathrm{v}_\infty = 450\ \mathrm{km/s}$.)

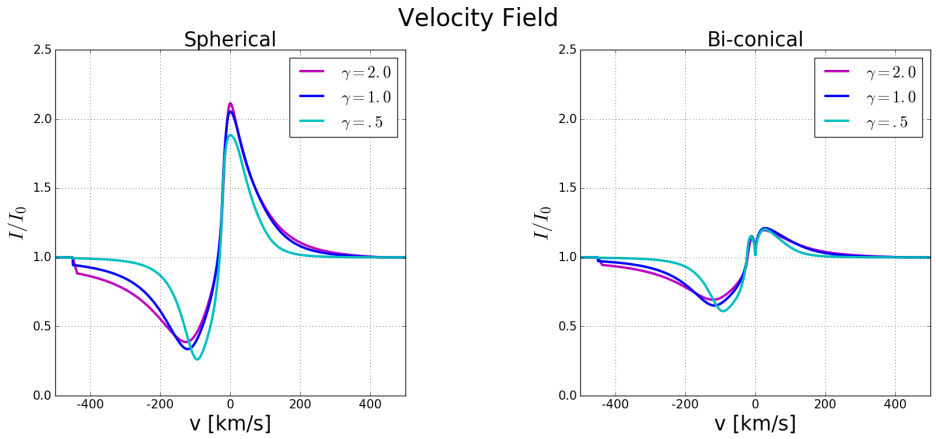

FIGURE 2.8: Velocity fields of power law index γ for spherical (left) and bi-conical (right) outflows. The bi-conical outflow used has geometry $(\alpha, \psi) = (45°, 45°)$. As γ increases, the terminal velocities are reached at progressively smaller distances and progressively larger densities, which results in stronger absorption for larger γ. For the bi-conical outflow, both how quickly the density grows with respect to the velocity field and the geometry will affect how much absorption/reemission occurs at a given observed velocity. (The remaining parameters used to generate the profiles are: $\tau_0 = 330, v_0 = 25$ km/s, $\mathrm{v}_\infty = 450$ km/s.)

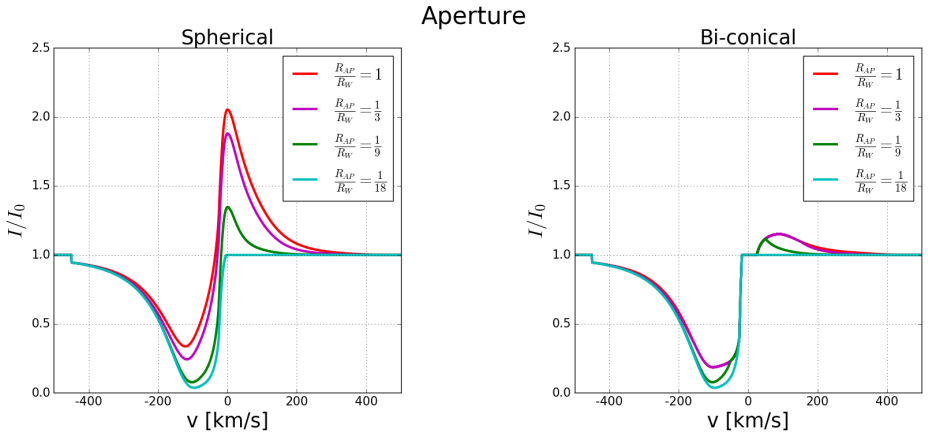

FIGURE 2.9: Limiting, circular, observing aperture. The ratio R_{AP}/R_W represents the fraction of the outflow (R_W) within a circular aperture (R_{AP}) centered on the source. At $R_{AP}/R_W = \frac{1}{18}$, the aperture is the same size as the source, i.e., $R_{AP} = R_{SF}$. The spherical model is shown to the left. As R_{AP} decreases, the emission profile diminishes rapidly. To the right is the bi-conical model with $\alpha = 45°$ and $\psi = 0°$. As R_{AP} decreases, the emission profile begins to diminish, however, the effect is less prominent compared to the spherical model. The majority of the wind lies along the line of sight and is not eminently affected by the decreasing aperture. (The remaining parameters used to generate the profiles are: $\tau_0 = 330, \gamma = 1, v_0 = 25$ km/s, $\mathrm{v}_\infty = 450$ km/s.)

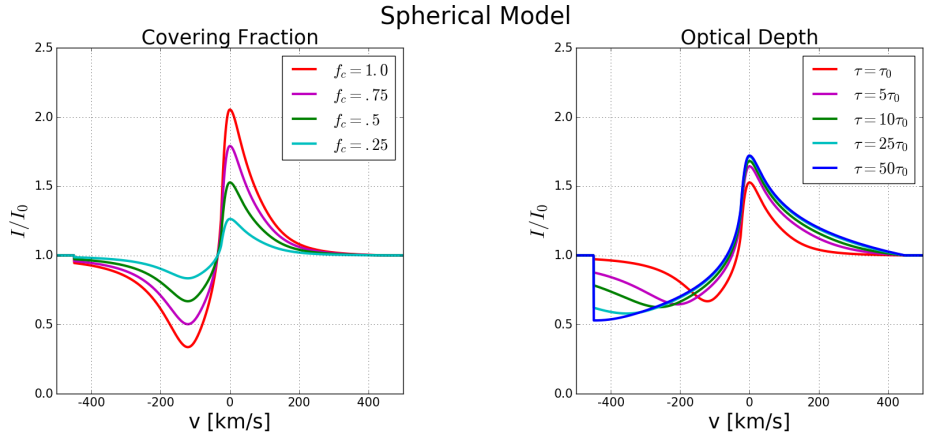

FIGURE 2.10: Spherical model with a constant covering fraction, f_c. In the left display, we vary the covering fraction. For $f_c = 1$, there are no holes/clumps in the wind and we recover the fiducial model. For $f_c = .2$, almost the entire wind has been removed leaving behind mostly continuum. Reducing f_c diminishes both the emission and absorption components. This is distinguishable from the effect of reducing the aperture, which reduces only emission. To the right, we fix $f_c = .5$, and allow the optical depth, τ, to vary as a multiple of τ_0. Increasing τ does lead to saturation in absorption like one usually expects, however, f_c will always leave a portion of the source uncovered, resulting in absorption components which do not reach zero. (The remaining parameters used to generate the profiles are: $\tau_0 = 330, \gamma = 1, v_0 = 25$ km/s, $\mathrm{v}_\infty = 450$ km/s.)

the bi-conical case example shown in Figure 2.9, where photons emitted by regions at progressively smaller projected velocities are blocked. Smaller apertures also help to reduce the contribution of the blue component of the scattered re-emission to the absorption profile (effect known as "in-filling", e.g., Prochaska, Kasen, and Rubin, 2011; Martin et al., 2012; Erb et al., 2012).

Recent works have advocated a covering fraction (f_c) smaller than unity for the neutral outflowing gas (Rivera-Thorsen et al., 2015; Jones et al., 2013). We have explored this possibility in Section 2.1, where we computed the profiles generated in a spherical outflow with varying f_c. The resulting line profiles are shown in Figure 2.10, left panel. The effect of a decreasing covering fraction is to reduce both the absorption and the scattered re-emission components. This effect is distinguishable from the changes introduced by different sized apertures, which act only to reduce the emission component (leaving the absorption untouched). A bi-conical outflow effectively covers only a fraction of the emitting source. The profiles resulting in the two cases (spherical with $f_c \neq 1$ and bi-conical), however, can clearly be distinguished, by the shape of the emission profile (e.g., the dip in the emission component at zero projected velocities, see Figure 2.7) and the ratio between the areas of the absorption and emission components. In the right panel of Figure 2.10, we fixed the covering fraction to $f_c = .5$ and explore how changing the optical depth, τ_0, changes the shape of the resulting profile. As the absorption saturates, i.e., $e^{-\tau} \to 0$ in I/I_0, the fraction of energy absorbed by a single shell $E(v) \to f_c$. The maximum possible depth of the absorption dip becomes $1 - f_c$ because a portion of the source always remains uncovered, allowing radiation to pass undisturbed directly to the observer.

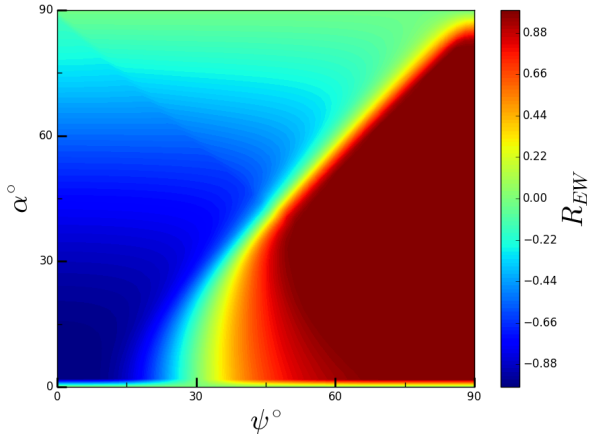

FIGURE 2.11: Map of the ratio $R_{EW} = \frac{A_{ABS}+A_{EM}}{|A_{ABS}|+A_{EM}}$, where A_{ABS} is the area below continuum, taken to be negative, and A_{EM} is the area above continuum, for winds of geometry with opening angle, α, and orientation angle, ψ. Winds with larger values of ψ are oriented away from the line of sight and become dominated by emission ($R_{EW} = 1$) for all but the largest values of α. In contrast, winds with smaller values of ψ are aligned with the line of sight and become dominated by absorption ($R_{EW} = -1$) for all but the largest values of α. Geometries approaching equivalent emission and absorption areas ($R_{EW} = 0$) include the spherical wind, i.e., $\alpha = 90°$, where $\alpha = \psi$, and where $\alpha = 0$ (by definition). (The remaining parameters used to generate the profiles are: $\tau_0 = 330, \gamma = 1, v_0 = 30$ km/s, $v_\infty = 500$ km/s.)

2.4.3 Equivalent Widths and Blue Emission In-fill

We next quantify the effects of the geometry on the ratio between the absorption and emission equivalent widths (EWs) of the model profiles. To do so, we directly compare the area produced by the light profile below the continuum, A_{ABS}, to the total area above the continuum, A_{EM} (which includes both the red and blue emission components). A_{ABS} is defined to be negative. To study the effect of the emission on the absorption profile as a function of the outflow geometry (α, ψ), we compute the ratio R_{EW} as follows:

$$R_{EW} = \frac{A_{ABS} + A_{EM}}{|A_{ABS}| + A_{EM}}. \tag{2.23}$$

The value of R_{EW} for different values of α and ψ is shown in Figure 2.11. In the spherical case, while ignoring occultation from the source, one would expect the profile to have equal absorption and emission EWs, or $R_{EW} = 0$ (e.g., Prochaska, Kasen, and Rubin, 2011). This is not always the case for bi-conical outflows. When viewed perpendicular to the line of sight (i.e., large values of ψ), a bi-conical outflow heavily favors emission, $(R_{EW} \approx 1)$, for all but the largest values of α. In contrast, when viewed directly along the line of sight (i.e., small values of ψ), the bi-conical outflow favors absorption, $(R_{EW} \approx -1)$, for all but the largest values of α. When the edge of the cone is aligned with the line of sight (i.e., $\alpha < 90°$ and $\alpha = \psi$) a large fraction of the source remains uncovered and the profile tends to have $R_{EW} \approx 0$. Small changes in either the orientation or the opening angles have large effects on R_{EW} in this regime. In addition, we also investigate how the outflow geometry directly affects the blue shifted emission in-filling of the absorption component in a P Cygni

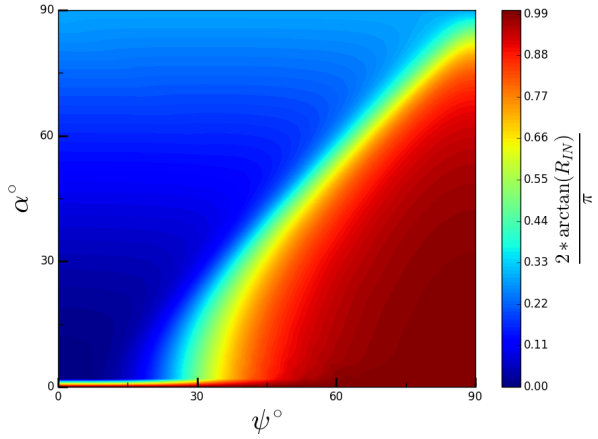

FIGURE 2.12: Map of the quantity $\frac{2*\arctan(R_{IN})}{\pi}$ for ratio $R_{IN} = \frac{A_{EM\setminus ABS}}{A_{ABS\setminus EM}}$, where $A_{EM\setminus ABS}$ is the blue shifted emission area, excluding the absorption component, and $A_{ABS\setminus EM}$ is the absorption area, excluding the emission component. Winds with larger values of ψ are oriented away from the line of sight and become dominated by emission ($R_{IN} >> 1$) for all but the largest values of α. In contrast, winds with smaller values of ψ are aligned with the line of sight and become dominated by absorption ($R_{IN} << 1$) for all but the largest values of α. (The remaining parameters used to generate the profiles are: $\tau_0 = 330, \gamma = 1, v_0 = 30$ km/s, $v_\infty = 500$ km/s.)

profile by allowing the geometry to vary while holding the remaining parameters constant in our models. We isolate the emission and absorption components, and consider the ratio:

$$R_{IN} = \frac{A_{EM\setminus ABS}}{A_{ABS\setminus EM}}, \tag{2.24}$$

where $A_{EM\setminus ABS}$ is the blue shifted emission area, excluding the absorption component, and $A_{ABS\setminus EM}$ is the absorption area, excluding the emission component. For $R_{IN} << 1$, there is barely any blue emission in-filling the absorption component of the profile. These outflows are characteristically oriented along the line of sight and have smaller opening angles. For $R_{IN} >> 1$, the profile is dominated by the emission component, and little to no absorption is visible in the profile. Such outflows are oriented away from the line of sight and have smaller opening angles. The later scenario is dramatically different from the blue emission in-filling present in spherical outflows, and unique to bi-conical outflows. As pointed out by Zhu et al. (2015), the blue emission in-fill can never dominate the absorption component in a spherical outflow. Ultimately, the exact value of the ratio R_{IN} will depend on all of the parameters mentioned in this paper, and additional factors such as multiple scattering, i.e., photons reemitted outside the resonant channel, but arguably the most important factor affecting R_{IN} is the geometry. We have plotted $(2/\pi)*\arctan(R_{IN})$ in Figure 2.12 to map the range of the ratio R_{IN} between zero and one. It is important to note that R_{IN} cannot be directly observed, for the blue infill and absorption areas will be combined in a P Cygni profile, i.e., $A_{EM\setminus ABS}$ + $A_{ABS\setminus EM}$. Therefore, only Figure 2.11, not Figure 2.12, can be compared to observations. However, the blue shifted emission infill can be separated from the true absorption component

using R_{IN}, from Figure 2.12, if model fits can sufficiently constrain the geometry of the outflow and the observed P Cygni profile. In the next section, we explore how reliably the outflow parameters can be recovered in simulated data.

2.5 Model Fitting

In this Section, we explore the accuracy at which the outflow parameters are recovered using spectral fitting procedures. To this aim, we created a set of 50 simulated spectra, with a range of randomly chosen input parameters. Our model is described by six parameters: the opening angle, α, the orientation angle, ψ, the power law index of the velocity field, γ, the optical depth, τ_o, the initial velocity, v_0, and the terminal velocity, v_∞. We generated the spectra by selecting parameters uniformly from the following parameter ranges: $20^\circ \leq \alpha \leq 90^\circ$, $0^\circ \leq \psi \leq 90^\circ$, $.5 \leq \gamma \leq 4$, $.01 \leq \tau_0 \leq 100$, $2 \leq v_0 \leq 80$ km/s, and $200 \leq v_\infty \leq 800$ km/s. In order to reproduce actual data, we added Gaussian noise to the simulated spectra, to reach a signal to noise ratio of approximately 10 in the normalized continuum (Henry et al., 2015).

To derive the best fit parameters for the model, we used the emcee package in python (Foreman-Mackey et al., 2013), which relies on the Python implementation of Goodman's and Weare's Affine Invariant Markov Chain Monte Carlo (MCMC) Ensemble sampler (Goodman and Weare, 2010). The emcee analysis returns probability distributions (PDFs) for each parameter. Because many of the PDFs are asymmetric, the best fit parameters were chosen to represent the most likely value (i.e., the mode) for a given parameter's PDF. Similarly, we chose the median of the absolute deviation around the mode (MAD) to describe the width for each distribution (and use this value as an estimate of the error associated with each parameter).

2.5.1 Discussion of Returned Parameters From Model Fitting

Figures 2.13, 2.14, and 2.15 show the comparison between the input parameter values (on the horizontal axis) and the recovered values (on the vertical axis). For clarity, we have organized the simulations according to orientation. In general, the parameters describing the geometry of the outflow (α,ψ) are the best constrained. The accuracy with which we derive the velocity and optical density parameters depends on the inclination of the cone with respect to the line of sight. The highest accuracy is reached for $30^\circ \leq \psi < 60^\circ$. These profiles are characterized by having both a strong emission and absorption component visible in the spectra, simultaneously providing constraints on the geometry, the velocity and the density of the scattering gas. When the cone is oriented almost perpendicularly to the line of sight (i.e., for $\psi > 60^\circ$), and for small opening angles, the profiles are dominated by the emission component. Additionally, the limited absorption present in these profiles is limited to material close to the emitting region, with low velocity and high density. Shells at higher velocities no longer contribute to the absorption – limiting their diagnostic power. In these cases, the terminal velocity v_∞ is not well constrained (i.e., measured with large uncertainties) and it is typically underestimated. This is because v_∞ has little effect on the emission component. Moreover, ψ itself appears to be overestimated. As demonstrated in Section 4, ψ acts to control the position of the emission component and a large change in ψ results in a small shift in the actual profile in terms of the observed velocities. This minuscule effect is difficult to detect with low signal-to-noise data.

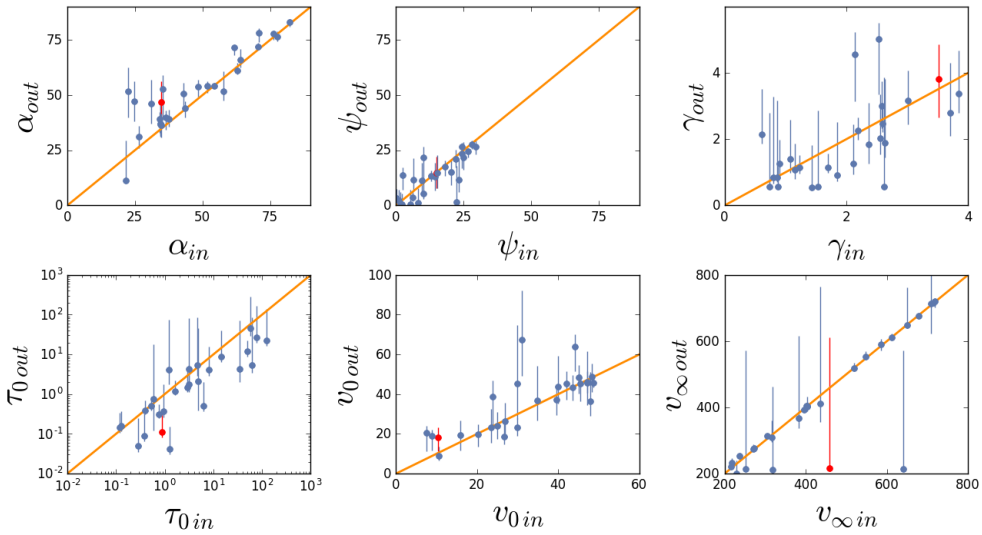

FIGURE 2.13: Returned parameters for the bi-conical model with orientation angle $0° \leq \psi < 30°$. The true value for a given parameter has been plotted along the horizontal axis while the best fit, or mode of the PDF, has been plotted along the vertical axis. The solid orange lines represent a perfect match between the true value and best fit. The top error bar represents the upper estimate of the median of the absolute deviation around the mode, and the bottom error bar represents the lower estimate of the median of the absolute deviation around the mode. These outflows are oriented along the line of sight. For sufficiently small opening angles, α, these profiles are characterized by a large absorption dip and a small emission spike. We have traced a profile that was drastically underestimated in v_∞ by coloring it red. The corresponding profile is shown in Figure 2.16.

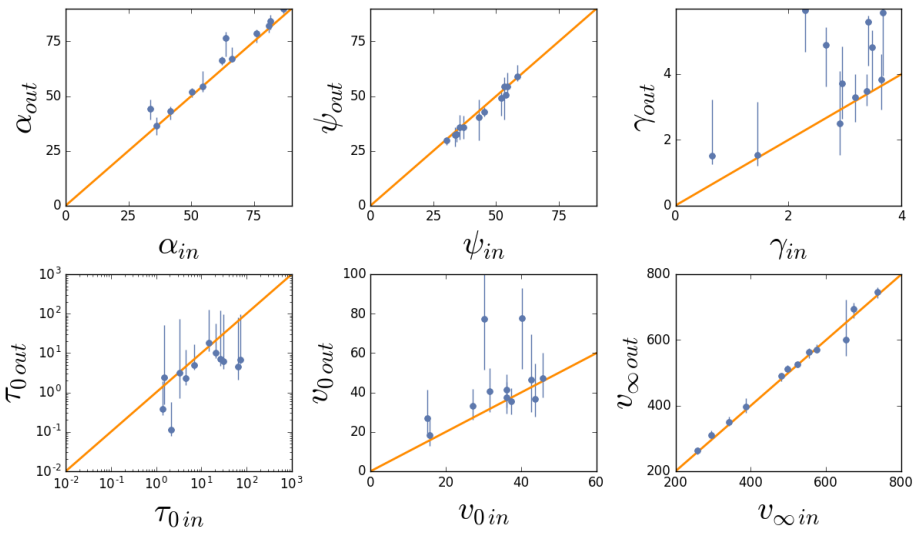

FIGURE 2.14: Returned parameters for the bi-conical model with orientation angle $30° \leq \psi < 60°$. The true value for a given parameter has been plotted along the horizontal axis while the best fit, or mode of the PDF, has been plotted along the vertical axis. The top error bar represents the upper estimate of the median of the absolute deviation around the mode, and the bottom error bar represents the lower estimate of the median of the absolute deviation around the mode. These profiles are characterized by having both strong absorption and emission components.

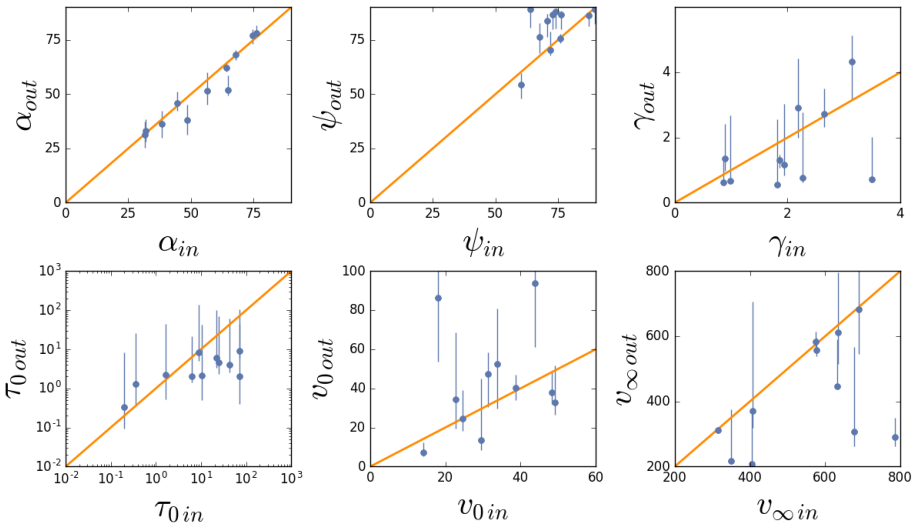

FIGURE 2.15: Returned parameters for the bi-conical model with orientation angle $60° \leq \psi \leq 90°$. The true value for a given parameter has been plotted along the horizontal axis while the best fit, or mode of the PDF, has been plotted along the vertical axis. The top error bar represents the upper estimate of the median of the absolute deviation around the mode, and the bottom error bar represents the lower estimate of the median of the absolute deviation around the mode. These outflows are perpendicular to the line of sight. For sufficiently small opening angles, α, these profiles are characterized by a small (if visible) absorption dip and a large emission spike.

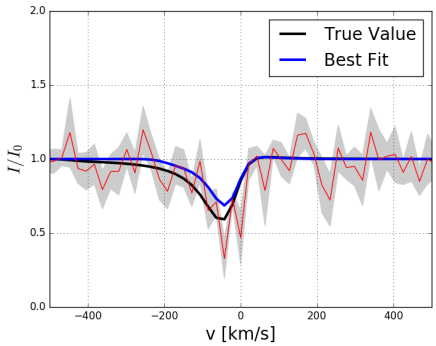

FIGURE 2.16: Mock profile (red), true value (black), and best fit (blue) for the red colored marker in Figure 2.13. The grey area represents plus or minus the error at each observed velocity. Here, the outflow is oriented toward the observer ($\psi < 30°$), and confined to the absorption region. Hence, the profile is dominated by an absorption dip with little to no visible emission. It is difficult for the model to find the correct terminal velocity, for the maximum velocity at which absorption occurs can easily succumb to the signal to noise.

When the cone is parallel to the line of sight, the parameters are typically well recovered, albeit with a larger uncertainty. We have selected one case, with drastically underestimated v_∞. The profile is plotted in Figure 2.16 and the simulation results are highlighted by the red point in Figure 2.13. It is easy to see that, because of the low column density of this particular example, the true velocity range of the absorption component has been lost due to the low signal-to-noise, resulting in an underestimate of v_∞.

2.6 Conclusion

In this chapter we have presented and discussed an extension to the SALT model presented in Scarlata & Panagia (2015), to calculate the expected absorption and re–emission line profile generated in a bi-conical outflow surrounding a galaxy with a finite size (R_{SF}), under the Sobolev approximation. We parametrize the outflow with the opening angle α and the inclination with respect to the line of sight. Similar to our previous work, we computed the analytical profiles for a gas velocity increasing with distance from the galaxy ($v \propto r^\gamma$), and a constant mass outflow rate ($n_l(r) \propto (vr^2)^{-1}$). We analyzed the effects of the wind geometry on the line profiles, and compared to the simpler spherical model, with constant covering fraction, f_c. The resulting profiles vary substantially. Depending on the orientation, the profile can vary from pure absorption (i.e., small α and ψ) to pure emission (for large ψ and small α), with a range of P Cygni-like profile shapes in between. We have studied how the ratio between the EW of the emission and absorption components changes with the outflow geometry. We used simulated spectra to study the accuracy and degeneracies in recovery of the outflow parameters from fitting models to the data. We show that for a typical S/N ratio of $\simeq 10$ in the continuum, the geometry can be accurately reproduced. The velocity field (described by v_0, v_∞, and γ) is better constrained when the terminal shell of the outflow intercepts the line of sight, producing absorption at v_∞. If this is not the case, then the maximum velocity remains largely unconstrained by the resulting absorption profiles. This fact has an

interesting consequence. Because the outflows will be distributed randomly in the sky, one would expect that for many of them gas moving at v_∞ will not necessarily contribute to the absorption component. Consequently, one would expect to find only weak correlations between the maximum velocity of absorption and galactic properties, as found by Martin et al. (e.g., 2012).

To conclude, by simultaneously modeling the resonant absorption and the associated resonant emission, the line profiles computed with our SALT model can be used to constrain the real 3-dimensional geometry and orientation of gaseous outflows, their density field and the velocity structure within the winds. This information can be used to constrain the wind launching mechanism, to ultimately shed light on SF driven feedback.

Chapter 3

Fitting to Green Pea Galaxies

3.1 Introduction and Data

In this chapter, we fit the SALT model developed in Chapter 2 to galactic data. We focus on individual atomic spectra as opposed to stacked data sets (Scarlata and Panagia, 2015). This will allow us to identify individual outflow geometries. Our data set consists of ten extremely high equivalent width emission line galaxies, known as 'Green Peas', originally selected from the Sloan Digital Sky Survey (SDSS) catalog by Cardamone et al. (2009). These ten galaxies were previously analyzed in the work of Henry et al. (2015) to study Lyα emission. We refer the reader to this paper for a more in depth overview of the data selection process and only provide the relevant details here. Observations were made using the Cosmic Origins Space (COS) spectrograph – aperture diameter $2.5''$ – aboard the Hubble Space Telescope (HST). The spectra were obtained in the far ultraviolet regime (FUV: $\lambda\,1340 - 1790$Å) across two different diffraction gratings, G130M and G160M, spanning $950 - 1450$Å for nine of the ten galaxies. For Galaxy 1424+4217, the G160M observation failed. The galaxies are compact and do not fill the COS aperture (200 km/s). Hence, they have a better resolution. The resolution for each grating was obtained from a line spread function (LSF). The FWHM of the LSF for G130M (G160M) corresponds to 25 (30) km/s for typical Green Peas and 37 (46) km/s for galaxy 1244+0216. Spectra obtained from both gratings are shown for galaxy 0303-0759 in Figure 3.3. Spectra for the remaining nine Green Peas can be obtained from Henry et al. (2015). For more information regarding the Green Peas see Tables 3.2 and 3.3. Throughout this chapter, we will assume the standard Big Bang cosmology, i.e., $H = 70$ km/s/Mpc, $\Omega_M = .3$ and $\Omega_\Lambda = .7$.

3.2 Data Fitting

The spectra were binned by 10 native COS pixels into one to reduce signal-to-noise (S/N) and mitigate the effects of correlated noise. We performed a linear fit to adjacent flux values near emission and absorption features, making sure to avoid the features themselves, to establish the continuum for normalization. Errors were taken from Henry et al. (2015). Our aim is to fit to transition lines in the Si II ion. In particular, we will fit to the $\lambda 1190.42$ and 1193.28Å Si II doublet. Both of these transitions have a fluorescent channel, i.e., once a photon is absorbed there is a probability that the electron can decay into an excited ground state, resulting in reemission at a higher wavelength. The relevant fluorescent lines are 1194.5 and 1197.39 for the $\lambda 1190.42$ and 1193.28Å transitions, respectively. A schematic for the Si II doublet is provided in Figure 3.2. The atomic information is provided in Table 3.1. To account for the fluorescent channel, we invoke the procedure for multiple scattering

discussed in Appendix A. The profile used for fitting with multiple scattering (MS) becomes

$$\begin{aligned} I(x)_{\mathrm{BC,MS}} = \quad & 1 - \int_{\max(x,1)}^{y_1} \frac{\Theta_{AP} * f_g * (1 - e^{-\tau(y)})}{y - y_{\min}} dy \\ + \quad & \int_{y_1}^{y_\infty} \frac{F_i * \Theta_{AP} * f_g * (1 - e^{-\tau(y)})}{2y} dy \\ + \quad & \int_{\max(x,1)}^{y_\infty} \frac{F_i * \Theta_{AP} * f_g * (1 - e^{-\tau(y)})}{2y} dy, \end{aligned} \tag{3.1}$$

where $F_i = F_F/F_R$ for the fluorescent/resonant channel, respectively. The red and blue emission component will now be distributed between both the resonant and fluorescent transition. Our fitting procedure is identical to the one proposed in Chapter 2 and we have assumed the same parameter ranges. The velocity at the aperture radius, v_{ap}, was determined using the ratio of the COS aperture radius, R_{AP}, i.e., the distance spanned by $1.25''$ at the angular diameter distance appropriate to each galaxy, with the Petrosian radius R_P (Petrosian, 1976). The ratio was then scaled by v_0 using the velocity field:

$$v_{ap} = v_0 \left(\frac{R_{AP}}{R_P} \right)^{\gamma}. \tag{3.2}$$

The best fit parameters and associated errors are provided in Table 3.4. The fits themselves are shown at the end of the Chapter. An emblem representing the best fit geometry has been provided in the upper left corner of each plot. The light blue features in the spectrums of galaxies 0303, 1133, and 1219 are known Milky Way contaminants have been removed from all model fits.

3.3 Conclusion

Galaxy 1137 represents the strongest case for a bi-conical geometry. The spectrum is characterized by very strong absorption features – almost reaching zero across the spectrum – and mild to weak emission features. Profiles with these characteristics are typical of galaxies observed face-on, which is supported by the best fit parameters: $(\alpha^\circ, \psi^\circ) = (64^\circ, 1^\circ)$. The only alternative explanation for such a profile is a spherical outflow with an aperture which fails to recover the full extent of the wind, resulting in a diminished emission component. However, the recovered initial velocity, v_0, and velocity power law index, γ, along with the associated Petrosian radius, R_P, suggest that this is not the case. Many of the galaxies favor an edge-on view, or $\alpha = \psi$ geometry. Galaxy 1424 – $(\alpha^\circ, \psi^\circ) = (72^\circ, 72^\circ)$ – is a strong example. In this scenario, a portion of the source always remains uncovered by the wind, allowing radiation to pass undisturbed directly to the observer. In these profiles, the depths of the absorption wells will not reach zero. For large enough α, the EWs associated with the absorption and emission components will be equal. Both of these characteristics can be explained by a spherical outflow with a constant covering fraction less than unity. Due to the frequent occurrence of these geometries, we expect that this is a more probable explanation for these galaxies. Realistically, both effects are likely at play. With improvements in our data fitting algorithm, we may be able to fit to the

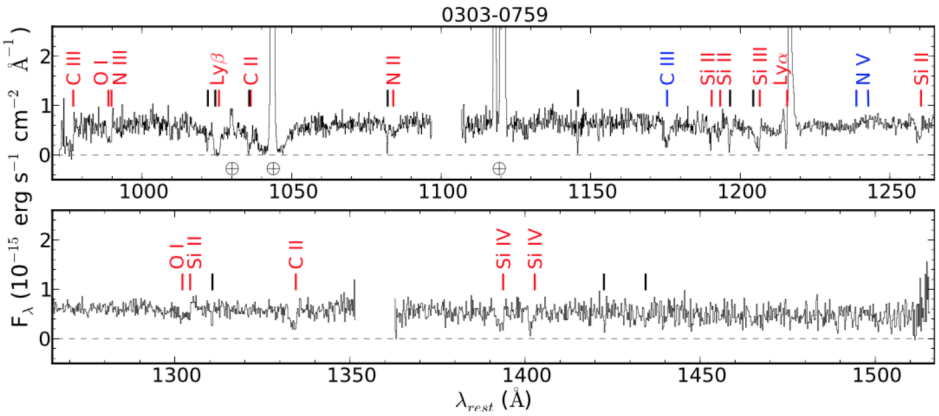

FIGURE 3.1: COS G130M + G160M spectrum of the Green Pea galaxy 0303-0759. Gaps in the spectrum demarcate the wavelengths between the COS FUV A and B segments. Red markers indicate the expected locations of ISM features in the Green Peas and blue labels show stellar features. Black vertical lines indicate Milky Way features, whereas $\bigoplus$ symbols mark geocoronal emission. This sight line contains damped Milky Way Lyα absorption, apparent around $\lambda_{rest} \approx 1042$ Å. Figure was taken from Henry et al. (2015).

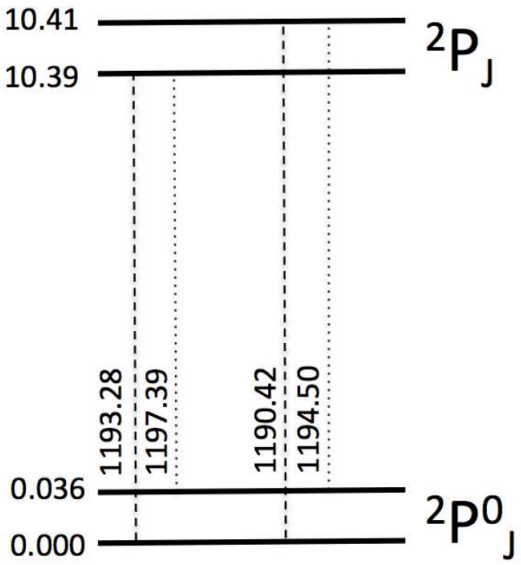

FIGURE 3.2: Si II doublet. (Figure taken from Scarlata and Panagia (2015).)

covering fraction along with the geometry, but at the present we are limited by computation time. An improved signal-to-noise may also help break the degeneracies. In the future, we plan to use the recovered parameters, including the geometry, to calculate galactic properties (e.g., mass outflow rate) for the Green Peas.

Guide written by —
Sunil Patel: www.sunilpatel.co.uk
Vel: LaTeXTemplates.com

TABLE 3.1: Atomic Data for Si II and Si III ions. Data taken from the NIST Atomic Spectra Database[a].

Ion	Vac. Wavelength Å	A_{ul} s^{-1}	f_{ul}	$E_l - E_u$ eV	$g_l - g_u$	Lower Level Conf.,Term,J	Upper Level Conf.,Term,J
Si II	1190.42	6.53×10^8	2.77×10^{-1}	$0.0 - 10.41520$	$2 - 4$	$3s^2 3p 2P^0 1/2$	$3s 3p^2 2P 3/2$
	1193.28	2.69×10^9	5.75×10^{-1}	$0.0 - 10.39012$	$2 - 2$	$3s^2 3p 2P^0 1/2$	$3s 3p^2 2P 1/2$
	1194.50	3.45×10^9	7.37×10^{-1}	$0.035613 - 10.41520$	$4 - 4$	$3s^2 3p 2P^0 3/2$	$3s 3p^2 2P 3/2$
	1197.39	1.40×10^9	1.50×10^{-1}	$0.035613 - 10.39012$	$4 - 2$	$3s^2 3p 2P^0 3/2$	$3s 3p^2 2P 1/2$
	1260.42	2.57×10^9	1.22	$0.0 - 9.836720$	$2 - 4$	$3s^2 3p 2P^0 1/2$	$3s^2 3d 2D 3/2$
	1264.73	3.04×10^9	1.09	$0.035613 - 9.838768$	$4 - 6$	$3s^2 3p 2P^0 3/2$	$3s^2 3d 2D 5/2$

[a] http://www.nist.gov/pml/data/asd.cfm

TABLE 3.2: Green Pea Galaxies 1

Galaxy	W_{H_α} (Å)	H_α/H_β	$E(B-V)_{\rm gas}$ (mag)	$\log(L_{H_\alpha}/\mathrm{erg\ s^{-1}})$	SFR $(M_\odot \mathrm{yr}^{-1})$	Log $M/M_\odot$	$12 + \log(0/H)$	$M_{\rm FUV}$ (mag)	β β	R_{UV} (kpc)
0303-0759	670	2.78	0.00	42.24	7.6	8.89	7.86	-20.35	-2.23	0.8
1244+0216	840	3.10	0.07	42.78	26.2	9.39	8.17	-20.32	-1.70	2.6
1054+5238	400	3.15	0.08	42.71	22.4	9.51	8.10	-21.31	-1.94	1.3
1137+3524	580	3.08	0.06	42.58	16.8	9.30	8.16	-20.56	-1.78	1.8
0911+1831	420	3.50	0.17	42.68	21.1	9.49	8.00	-20.56	-1.82	1.1
0926+4427	610	3.20	0.10	42.49	13.6	8.52	8.01	-20.58	-1.98	1.0
1424+4217	1100	3.01	0.04	42.57	16.5	8.08	8.04	-20.40	-1.90	1.0
1133+6514	300	2.90	0.01	42.02	4.6	9.04	7.97	-20.40	-1.93	1.9
1249+1234	670	3.09	0.07	42.50	13.8	8.79	8.11	-20.25	-1.82	1.8
1219+1526	1270	2.87	0.00	42.43	11.9	8.09	7.89	-19.94	-1.65	0.7

TABLE 3.3: Green Pea Galaxies 2

Galaxy	RA (J2000)	DEC (J2000)	z	$E(B-V)_{\rm MW}$ (mag)	Rest Wavelength Coverage (Å)	G130 Exposure (s)	G160 Exposure (s)
0303-0759	03 03 21.41	-07 59 23.2	0.164887	0.0877	975 - 1515	2190	3829
1244+0216	12 44 23.37	02 15 40.4	0.239420	0.0213	945-1430	2042	6507
1054+5238	10 53 30.80	52 37 52.9	0.252645	0.0132	910-1425	824	2736
1137+3524	11 37 22.14	35 24 26.7	0.194396	0.0161	965-1505	1264	2340
0911+1831	09 11 13.34	18 31 08.2	0.262236	0.0248	900-1435	2074	6530
0926+4427	09 26 00.44	44 27 36.5	0.180698	0.0165	970-1505	5640	6180
1424+4217	14 24 05.72	42 16 46.3	0.184800	0.0094	965-1220	1209	0[a]
1133+6514	11 33 03.80	65 13 41.4	0.241400	0.0097	945-1430	1232	4589
1249+1234	12 48 34.63	12 34 02.9	0.263403	0.0252	900-1425	1644	6372
1219+1526	12 19 03.98	15 26 08.5	0.195614	0.0239	965-1505	716	2304

[a] Failed Observation

TABLE 3.4: Best Fits with α and ψ

Galaxy		α (deg)	ψ (deg)	γ	$\tau_{\rm o}$	v_0 (km/s)	$v_{\rm w}$ (km/s)	$v_{\rm ap}$ (km/s)
0911+1831	Mode	78^{+4}_{-14}	63^{+12}_{-7}	$1.2^{+.3}_{-.3}$	$1.7^{+6}_{-.4}$	17^{+14}_{-4}	550^{+47}_{-27}	98
0303-0759		39^{+9}_{-9}	31^{+7}_{-9}	$1.7^{+0.1}_{-0.4}$	$0.3^{+3}_{-0.2}$	31^{+16}_{-12}	708^{+20}_{-166}	394
1054+5238		45^{+7}_{-5}	46^{+8}_{-9}	$0.7^{+0.6}_{-0.07}$	$0.4^{+4}_{-0.2}$	22^{+21}_{-6}	717^{+19}_{-170}	53
0926+4427		51^{+3}_{-2}	55^{+3}_{-2}	$1.8^{+.07}_{-2}$	$3^{+36}_{-0.8}$	11^{+5}_{-1}	951^{+21}_{-290}	129
1244+0216		$90^{+0.07}_{-2}$	83^{+3}_{-43}	$2^{+0.004}_{-0.2}$	14^{+25}_{-5}	15^{+2}_{-4}	270^{+27}_{-13}	301
1137+3524		64^{+12}_{-8}	1^{+19}_{-4}	$1.4^{+.2}_{-.2}$	19^{+30}_{-6}	$5^{+2}_{-.6}$	711^{+118}_{-5}	30
1424+4217		72^{+5}_{-11}	72^{+4}_{-17}	$0.7^{+0.2}_{-0.1}$	0.8^{+13}_{-1}	47^{+18}_{-14}	694^{+61}_{-138}	127
1249+1234		87^{+1}_{-12}	87^{+1}_{-13}	$1.0^{+0.2}_{-0.2}$	11^{+24}_{-3}	15^{+8}_{-3}	757^{+44}_{-15}	44
1133+6514		39^{+11}_{-10}	55^{+13}_{-10}	$0.5^{+0.7}_{-0.02}$	$0.3^{+5}_{-0.02}$	52^{+33}_{-23}	286^{+385}_{-11}	86
1219+1526		16^{+11}_{-3}	20^{+10}_{-6}	$2.0^{+.02}_{-.7}$	2^{+22}_{-1}	25^{+31}_{-7}	729^{+90}_{-100}	> 729

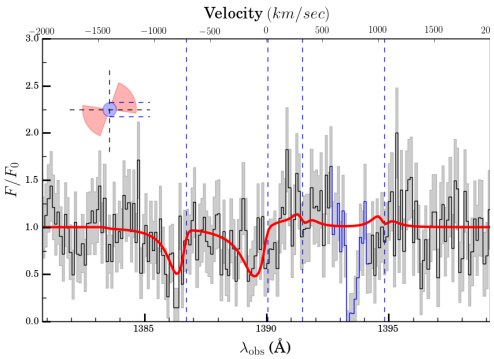

FIGURE 3.3: 0303

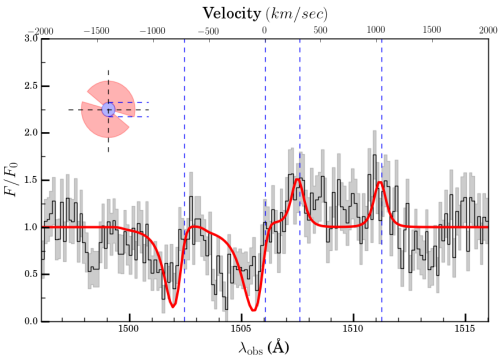

FIGURE 3.4: 0911

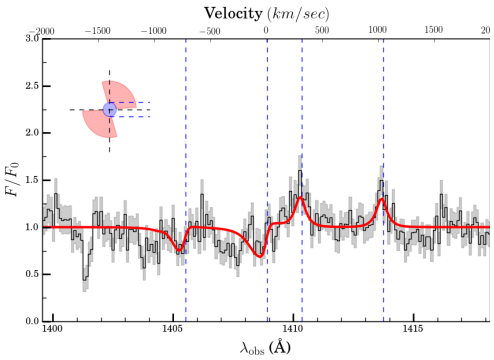

FIGURE 3.5: 0926

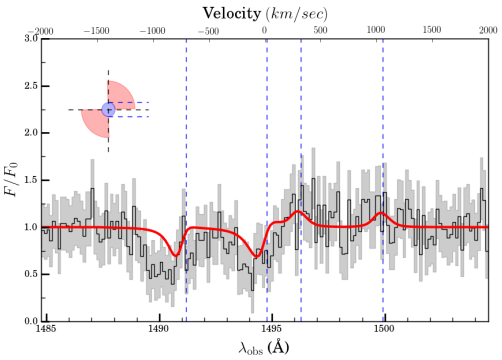

FIGURE 3.6: 1054

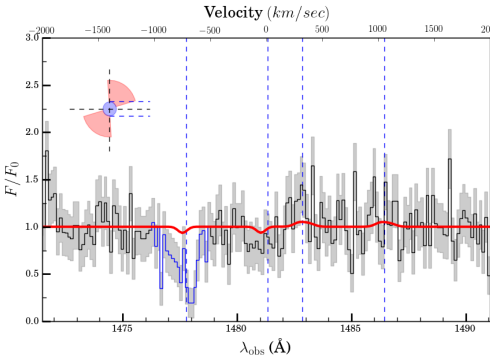

FIGURE 3.7: 1133

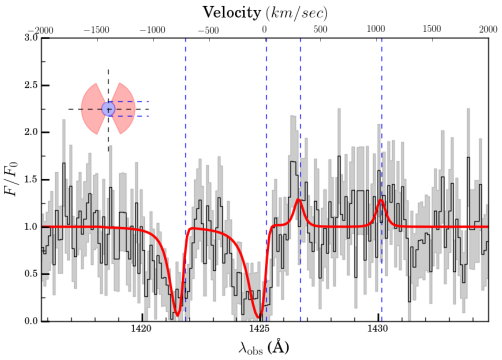

FIGURE 3.8: 1137

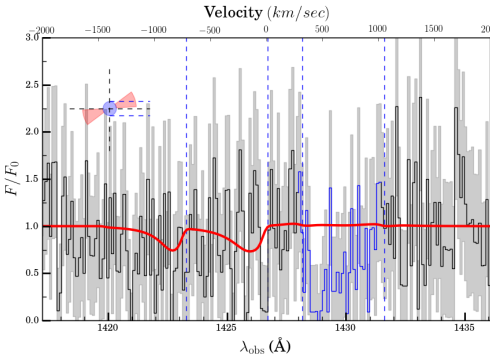

FIGURE 3.9: 1219

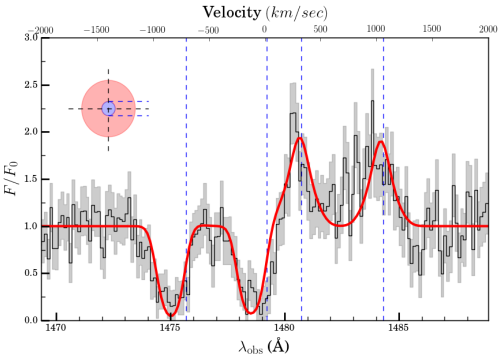

FIGURE 3.10: 1244

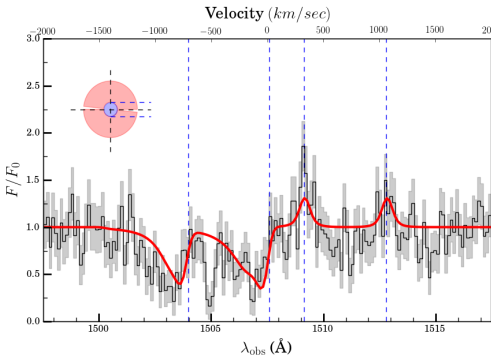

FIGURE 3.11: 1249

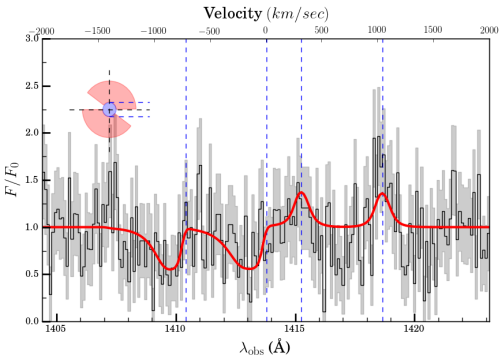

FIGURE 3.12: 1424

Appendix A

Multiple Scattering

Here we review the method of multiple scattering by Scarlata and Panagia (2015). Once a resonant photon is scattered/absorbed it will have a probability of getting re-absorbed/re-scattered by local ions. We define the escape probability β of a photon from a shell of velocity v to be the probability that a photon is scattered/absorbed at resonance per mean free path, i.e.,

$$\beta = \frac{1 - e^{-\tau(v)}}{\tau}. \tag{A.1}$$

Once a photon is scattered, it will have a probability p_F of being re-emitted via the fluorescent channel and a probability p_R of being re-emitted via the resonant channel. Because of the Sobolev approximation, a photon emitted via the fluorescent channel will escape the outflow and make its way to the observer. Of the fraction p_R, a fraction $1 - \beta$ of photons will be absorbed again before they escape the shell. Accordingly, some of these photons will enter the resonant channel and some the fluorescent channel. The process repeats itself iteratively. The final fraction of photons entering the fluorescent channel becomes

$$F_F(\tau) = p_F/[1 - p_R(1 - \beta)], \tag{A.2}$$

and the final fraction entering the resonant channel becomes

$$F_R(\tau) = \beta p_R/[1 - p_R(1 - \beta)]. \tag{A.3}$$

After each scattering, the optical depth will depend upon the velocity and the new trajectory of the scattered photon. To account for this, we take β in expressions A.2 and A.3 averaged over the 2-sphere,

$$\oint \beta d\Omega = \frac{1}{4\pi} \int \beta d(\cos\theta) d\phi. \tag{A.4}$$

Appendix B

Observing Aperture

To account for a limiting, observing aperture we need to make precise when a shell in an outflow will no longer contribute to the observed spectrum. For a given v_{obs}, we define the curve of constant observed velocity, Γ, to be the intersection of the surface of constant v_{obs} with the ξs-plane. We have plotted Γ for several velocity fields of different power law index γ to the right in Figure B.1. Shells that intersect Γ outside of the aperture radius, ρ_{AP}, will no longer contribute to the observed spectrum at v_{obs}.

We seek to parameterize Γ in the ξs-plane. To this end, we consider the generic problem of identifying the curve of constant observed velocity between two shells of known position in a velocity field of arbitrary power law as defined in Section 2. Let ρ_1, v_1 and ρ_2, v_2 be the radii and velocities, respectively, for two separate shells such that $\rho_2 > \rho_1$. See Figure B.1. Finding the equivalent observed velocity to v_1 at ρ_2, we get

$$v_1 = v_2 \cos\theta \tag{B.1}$$

$$\implies \cos\theta = \frac{v_1}{v_2} = \left(\frac{\rho_1}{\rho_2}\right)^{\gamma}. \tag{B.2}$$

We want to exclude all shells along the curve of constant observed velocity that fall outside the aperture radius, ρ_{AP}, hence, we seek the location of constant observed velocity in terms of position. Using the angle determined from the velocity field, we define a triangle in terms of the radius, ρ_2, such that $\rho_{2,s}^2 + \rho_{2,\xi}^2 = \rho_2^2$, where $\rho_{2,s} = \rho_2 \cos\theta$ and $\rho_{2,\xi} = \rho_2 \sin\theta$ are the horizontal and vertical components of the triangle, respectively. Moreover,

$$\frac{\rho_{2,s}}{\rho_2} = \left(\frac{\rho_1}{\rho_2}\right)^{\gamma} \tag{B.3}$$

$$\implies \rho_{2,s} = \rho_1^{\gamma}\rho_2^{1-\gamma}. \tag{B.4}$$

Hence, the vertical component becomes

$$\rho_{2,\xi} = [\rho_2^2 - \rho_1^{2\gamma}\rho_2^{2(1-\gamma)}]^{1/2}. \tag{B.5}$$

Thus, the parameterization of Γ in the ξs-plane becomes

$$\Gamma = (\xi, s) = (\rho_1^{\gamma}\rho_2^{1-\gamma}, [\rho_2^2 - \rho_1^{2\gamma}\rho_2^{2(1-\gamma)}]^{1/2}) \tag{B.6}$$

$$= (xy^{(1-\gamma)/\gamma}, [y^{2/\gamma} - x^2 y^{2(1-\gamma)/\gamma}]^{1/2}), \tag{B.7}$$

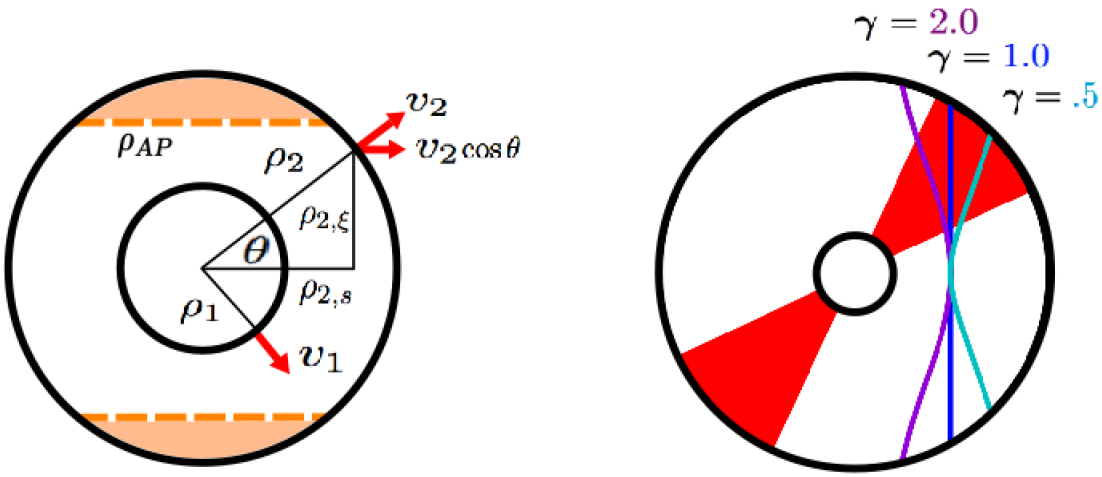

FIGURE B.1: On the left are concentric shells of radii ρ_1 and ρ_2 at velocities v_1 and v_2, respectively. The orange regions are excluded by an aperture of radius ρ_{AP}. For a shell of velocity v_1, the equivalent observed velocity for a shell with larger radius, ρ_2, is defined by the expression, $v_1 = v_2 \cos\theta$. We want to find this location in terms of position, hence, we use the angle θ to construct a right triangle in terms of the radius, ρ_2, i.e., $\rho_2^2 = \rho_{2,s}^2 + \rho_{2,\xi}^2$, where $\rho_{2,s} = \rho_2 \cos\theta$ and $\rho_{2,\xi} = \rho_2 \sin\theta$ are the horizontal and vertical components of the triangle, respectively. A shell will be excluded by the aperture if the location of constant observed velocity lies outside the aperture radius, i.e. $\rho_{2,\xi} > \rho_{AP}$. To the right are curves, Γ, of constant observed velocity, v_{obs}, for velocity fields of different power law index, γ, drawn overtop a bi-conical outflow shown in red. These curves represent where the surfaces of constant observed velocity intersect the plane of the diagram. If a shell intersects the curve, it will contribute to the spectrum at the observed velocity defining Γ.

where in the last expression we have converted back into velocity and expressed the generic quantities in terms relevant to the paper. Thus, following along the curve of constant observed velocity for a shell of radius ρ_1 and velocity v_1, all contributions to the spectrum at the observed velocity v_1 from shells of larger radius, ρ_2, will be excluded if $\rho_{AP} < \rho_{2,\xi}$, i.e.,

$$\rho_{AP} < [\rho_2^2 - \rho_1^{2\gamma}\rho_2^{2(1-\gamma)}]^{1/2}. \tag{B.8}$$

Converting to velocity and the relevant quantities, we get the following condition,

$$y_{ap} < [y^{2/\gamma} - x^2 y^{2(1-\gamma)/\gamma}]^{\gamma/2}, \tag{B.9}$$

where $y_{ap} = v_{ap}/v_0$. Therefore, we define the aperture factor

$$\Theta_{AP} \quad := \quad \Theta(y_{\rm ap} - [y^{2/\gamma} - x^2 y^{2(1-\gamma)/\gamma}]^{\gamma/2}), \tag{B.10}$$

where Θ is the Heaviside function:

$$\Theta := \begin{cases} 0 & \text{if } \ \mathrm{y_{ap}} < [\mathrm{y}^{2/\gamma} - \mathrm{x}^2\mathrm{y}^{2(1-\gamma)/\gamma}]^{\gamma/2} \\ \\ 1 & \mathrm{otherwise.} \end{cases} \tag{B.11}$$

This scaling factor will exclude all shells outside the aperture radius. Note that this construction will work for all outflow geometries.

Appendix C

Geometric Factor

To calculate the geometric factor, f_g, we want to find the fraction of a bi-conical shell of intrinsic velocity, y, overlapping the constant observed velocity contour of interest from the corresponding spherical shell. For a velocity field of power law index, γ, the curve of constant observed velocity, x, will be

$$\Gamma = (\xi, s) = (xy^{(1-\gamma)/\gamma}, [y^{2/\gamma} - x^2 y^{2(1-\gamma)/\gamma}]^{1/2}).$$

See Appendix A for a derivation. All shells that intersect, Γ, will contribute to the spectrum at x. Thus for a given x, we want to compute f_g for all shells of intrinsic velocity, y, that intersect Γ. Then given a shell of intrinsic velocity, y, the distance to the relevant contour from the center of the outflow, written in terms of velocity, will be $V = xy^{(1-\gamma)/\gamma}$. This distance has been drawn in orange in Figure C.1.

Now that we know the precise location of the observed velocity contour in terms of x, we need to explicitly compute, f_g. Our approach will be to find the angular separation, η, made by half of the arc length of the overlap of the spherical shell with the observed velocity contour, shown in dark blue. We consider four major cases regarding the wind geometry.

For cases I and II: $\alpha + \psi > 90^\circ$ and $\alpha > \psi$ (I) or $\alpha < \psi$ (II). As shown in I, the observed velocity contour touches both the front and backside of the bi-conical shell. We will distinguish these contributions as f_{gu} and f_{gl}, respectively. We provide only the pictorial representation of the geometry necessary to calculate f_{gu}, however, calculations for both f_{gu} and f_{gl} are provided. We will need the following quantities to compute f_{gu}:

$$\begin{aligned}
\delta &= \pi/2 - \alpha;\ \beta = \alpha + \psi - \pi/2; \\
W_1 &= \frac{y \sin(\beta)}{\sin(\pi - \psi)};\ W_2 = \frac{V}{\sin(\psi)};\ W = W_1 + W_2; \\
P &= \frac{W \sin(\delta)}{\sin(\alpha + \psi)};\ S = y^{1/\gamma};\ Q = S \sin(\alpha);\ T = (Q^2 - [Q - W]^2)^{1/2}; \\
K &= \frac{V}{\tan(\psi)};\ J = \frac{P}{\tan(\beta)};\ G = J - K;\ \eta = \arctan\left(\frac{T}{G}\right).
\end{aligned}$$

Thus,

$$f_{gu} = \frac{\eta}{\pi}$$

(If $V > J \tan(\psi)$, set $G = K - J$ and take $f_{gu} = 1 - \frac{\eta}{\pi}$.)

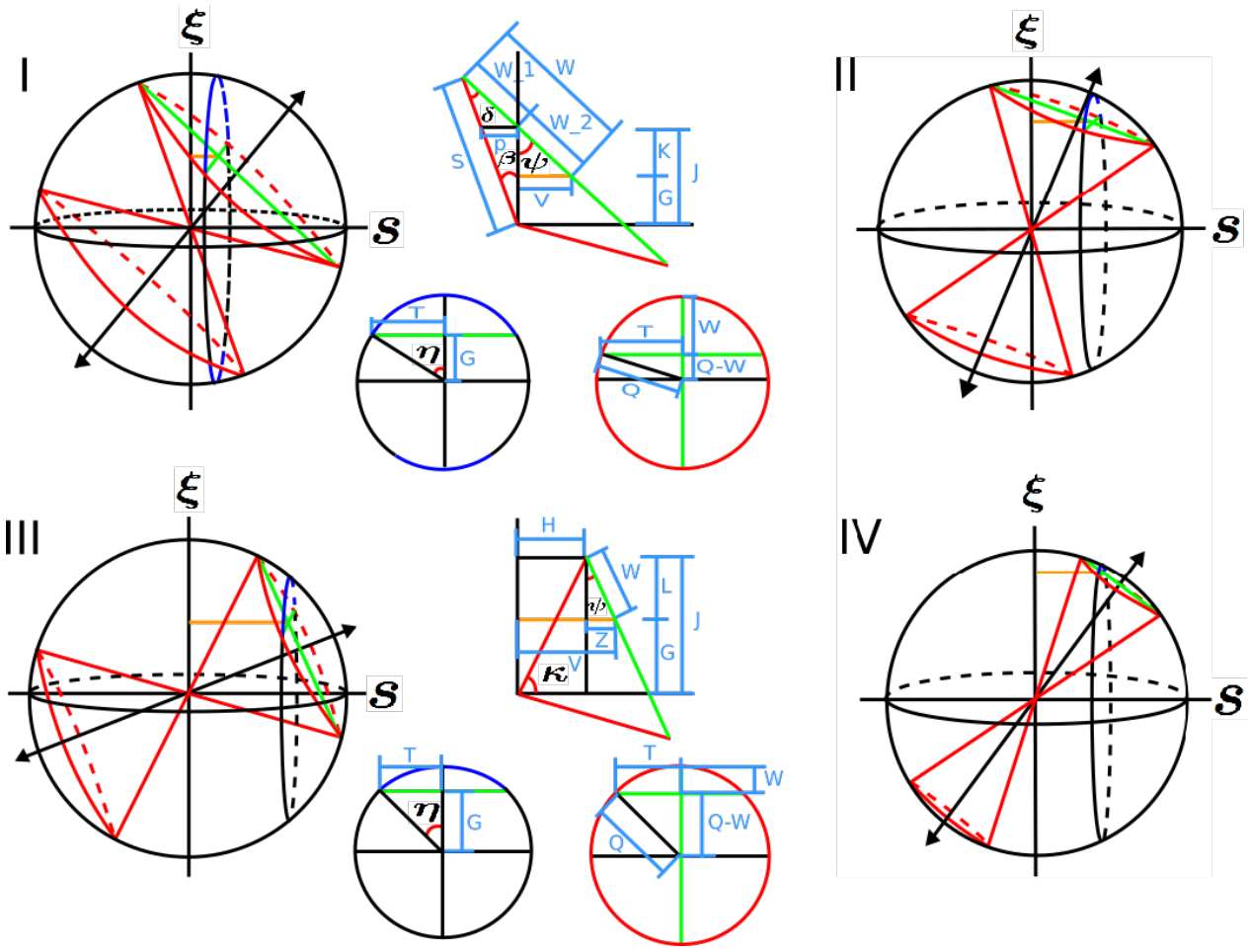

FIGURE C.1: Diagram containing various geometries and orientations of the bi-conical outflow: (I) $\alpha + \psi > 90°$ and $\alpha > \psi$, (II) $\alpha + \psi > 90°$ and $\alpha < \psi$, (III) $\alpha + \psi < 90°$ and $\alpha > \psi$, and (IV) $\alpha + \psi < 90°$ and $\alpha < \psi$. We want to find the fraction of the bi-conical shell overlapping the spherical shell for a given observed velocity. We use the band contour of constant observed velocity for a shell of velocity y located at a distance $V = xy^{(1-\gamma)/\gamma}$ from the ξ-axis. Our goal to compute f_g, is to calculate the angular separation, η, made by half of the arc length of the overlap of the spherical shell with the observed velocity contour, shown in dark blue. To do this, we calculate the two lengths, T and G, forming the tangent of η. To complete this task, we calculate T from the circle formed by the intersection of the bi-conical shell with the spherical shell, shown in red. We have shown the necessary values for calculating η in I and II. The computation for III, is the same as I, and the computation for IV, follows from III.

To compute f_{gl}, we will need the following:

$$\begin{aligned} N &= \frac{V}{\sin\psi};\ L = W_1 - N;\ T = [Q^2 - (Q-L)^2]^{1/2}; \\ H &= \frac{V}{\tan\psi};\ G = J + H;\ \eta = \arctan\left(\frac{T}{G}\right). \end{aligned}$$

Thus,

$$f_{gl} = \frac{\eta}{\pi}.$$

Therefore,

$$f_g = f_{gu} + f_{gl}.$$

For cases III and IV: $\alpha + \psi < 90^\circ$ and $\alpha > \psi$ (III) or $\alpha < \psi$ (IV). We will need the following quantities to compute f_g:

$$\begin{aligned} \kappa &= \alpha + \psi;\ H = y^{1/\gamma}\cos(\kappa);\ Z = V - H;\ W = \frac{Z}{\sin(\psi)};\ L = \frac{Z}{\tan(\psi)}; \\ J &= y^{1/\gamma}\sin(\kappa);\ Q = S\sin(\alpha);\ G = J - L;\ T = [Q^2 - (Q-W)^2]^{1/2}; \\ \eta &= \arctan\left(\frac{T}{G}\right). \end{aligned}$$

Therefore,

$$f_g = \frac{\eta}{\pi}.$$

(If $V > J\tan(\psi) + H$, set $G = L - J$ and take $f_g = 1 - \frac{\eta}{\pi}$.)

Bibliography

Ambartsumian, Viktor Amazaspovich (1958). "Theoretical astrophysics." In: *New York, Pergamon Press [1958]*.

Bae, Hyun-Jin and Jong-Hak Woo (2016). "The Prevalence of Ionized Gas Outflows in Type 2 AGNs II. 3-D Biconical Outflow Models". In: *arXiv preprint arXiv:1606.05348*.

Beals, C. S. (1929). "On the nature of Wolf-Rayet emission". In: 90, pp. 202–212. DOI: 10.1093/mnras/90.2.202.

— (1931). "The contours of emission bands in novæ and Wolf-Rayet stars". In: 91, pp. 966–977. DOI: 10.1093/mnras/91.9.966.

Campbell, W. W. (1892). "The spectrum of Nova AurigÃ in February and March, 1892". In: *Astronomy and Astro-Physics (formerly The Sidereal Messenger)* 11, pp. 799–811.

Cardamone, C. et al. (2009). "Galaxy Zoo Green Peas: discovery of a class of compact extremely star-forming galaxies". In: 399, pp. 1191–1205. DOI: 10.1111/j.1365-2966.2009.15383.x. arXiv: 0907.4155.

Castor, John I (1970). "Spectral line formation in Wolf–Rayet envelopes". In: *Monthly Notices of the Royal Astronomical Society* 149.2, pp. 111–127.

Chisholm, J. et al. (2016). "A Robust Measurement of the Mass Outflow Rate of the Galactic Outflow from NGC 6090". In: *ArXiv e-prints*. arXiv: 1605.05769.

Erb, Dawn K (2015). "Feedback in low-mass galaxies in the early Universe". In: *arXiv preprint arXiv:1507.02374*.

Erb, Dawn K. et al. (2012). "Galactic Outflows in Absorption and Emission: Near-UV Spectroscopy of Galaxies at 1<z<2". In: *Astrophys. J.* 759, p. 26. DOI: 10.1088/0004-637X/759/1/26. arXiv: 1209.4903 [astro-ph.CO].

Foreman-Mackey, Daniel et al. (2013). "emcee: The MCMC hammer". In: *Publications of the Astronomical Society of the Pacific* 125.925, p. 306.

Goodman, Jonathan and Jonathan Weare (2010). "Ensemble samplers with affine invariance". In: *Communications in applied mathematics and computational science* 5.1, pp. 65–80.

Henry, A. et al. (2015). "Lyα Emission from Green Peas: The Role of Circumgalactic Gas Density, Covering, and Kinematics". In: 809, 19, p. 19. DOI: 10.1088/0004-637X/809/1/19. arXiv: 1505.05149.

Jones, Tucker A et al. (2013). "Keck spectroscopy of gravitationally lensed z? 4 galaxies: Improved constraints on the escape fraction of ionizing photons". In: *The Astrophysical Journal* 779.1, p. 52.

Krumholz, Mark R et al. (2017). "The Observable Properties of Cool Winds from Galaxies, AGN, and Star Clusters. I. Theoretical Framework". In: *arXiv preprint arXiv:1702.05102*.

Kudritzki, Rolf P (2002). "Line-driven winds, ionizing fluxes, and ultraviolet spectra of hot stars at extremely low metallicity. I. Very massive O stars". In: *The Astrophysical Journal* 577.1, p. 389.

Lamers, H. J. G. L. M. and J. P. Cassinelli (1999). *Introduction to Stellar Winds*, p. 452.

Martin, C. L. et al. (2012). "Demographics and Physical Properties of Gas Outflows/Inflows at 0.4 z 1.4". In: 760, 127, p. 127. DOI: 10.1088/0004-637X/760/2/127. arXiv: 1206.5552.

Martin, Crystal L et al. (2013). "SCATTERED EMISSION FROM z 1 GALACTIC OUTFLOWS". In: *The Astrophysical Journal* 770.1, p. 41.

Parker, E. N. (1958). "Dynamics of the Interplanetary Gas and Magnetic Fields." In: 128, p. 664. DOI: 10.1086/146579.

Petrosian, V. (1976). "Surface brightness and evolution of galaxies". In: 209, pp. L1–L5. DOI: 10.1086/182253.

Prochaska, J. X., D. Kasen, and K. Rubin (2011). "Simple Models of Metal-line Absorption and Emission from Cool Gas Outflows". In: 734, 24, p. 24. DOI: 10.1088/0004-637X/734/1/24. arXiv: 1102.3444.

Rivera-Thorsen, Thøger E et al. (2015). "The Lyman Alpha Reference Sample. V. The Impact of Neutral ISM Kinematics and Geometry on Lyα Escape". In: *The Astrophysical Journal* 805.1, p. 14.

Rybicki, George B and Alan P Lightman (2008). *Radiative processes in astrophysics*. John Wiley & Sons.

Scarlata, C. and N. Panagia (2015). "A Semi-analytical Line Transfer Model to Interpret the Spectra of Galaxy Outflows". In: *Astrophys. J.* 801.1, p. 43. DOI: 10.1088/0004-637X/801/1/43. arXiv: 1501.07282 [astro-ph.GA].

Scuderi, S et al. (1992). "H-alpha observations of early-type stars". In: *The Astrophysical Journal* 392, pp. 201–208.

Shopbell, PL and J Bland-Hawthorn (1998). "The asymmetric wind in M82". In: *The Astrophysical Journal* 493.1, p. 129.

Sobolev, Viktor Viktorovich (1960). "Moving envelopes of stars". In: *Cambridge: Harvard University Press, 1960* 1.

Veilleux, Sylvain, Gerald Cecil, and Joss Bland-Hawthorn (2005). "Galactic winds". In: *Ann. Rev. Astron. Astrophys.* 43, pp. 769–826. DOI: 10.1146/annurev.astro.43.072103.150610. arXiv: astro-ph/0504435 [astro-ph].

Zhu, Guangtun Ben et al. (2015). "Near-ultraviolet Spectroscopy of Star-forming Galaxies from eBOSS: Signatures of Ubiquitous Galactic-scale Outflows". In: *The Astrophysical Journal* 815.1, p. 48.